

1 A Twenty-Year Dynamical Oceanic Climatology: 1994-2013.
2 Part 1: Active Scalar Fields: Temperature, Salinity, Dynamic
3 Topography, Mixed-Layer Depth, Bottom Pressure

4 *Draft Version 1.2**

5 The ECCO Consortium (M. Buckley⁸, J.-M. Campin³, A. Chaudhuri¹, I. Fenty²,
6 G. Forget³, I. Fukumori²,
7 P. Heimbach^{3,4}, C. Hill³, C. King³, X. Liang⁵, A. Nguyen⁴
8 C. Piecuch¹, R. Ponte¹, K. Quinn¹,
9 M. Sonnewald³, D. Spiegel³, N. Vinogradova⁷, O. Wang², C. Wunsch^{3,6})[†]

10 March 1, 2017

11 **Abstract**

12 The World Ocean Circulation Experiment (WOCE) was created to produce the first cli-
13 matologically useful picture of the ocean circulation and its low-frequency variability. This
14 goal is addressed here from the state estimate of the Estimating the Circulation and Climate
15 of the Ocean (ECCO) consortium, which uses almost all of the data obtained during WOCE
16 and its aftermath along with the much improved general circulation modeling capabilities.
17 A dynamically and data-consistent, time-evolving, state estimate is available depicting the
18 ocean and its ice-cover over a 23-year time-span, globally, from the sea surface to the sea
19 floor. The resulting time-dependent 20-year long climatology includes temperature, salinity,
20 surface elevation, bottom pressure, sea-ice, and three components of velocity. Accompany-
21 ing the state estimate are modified estimates of meteorological forcing-fields, ocean interior
22 mixing coefficients, and initial conditions. Much spatial structure persists through the two-
23 decade averaging. Results here are primarily pictorial in nature, intended to give the wider
24 community a sense of what is now available and useful and where more detailed analysis
25 would be fruitful. An extended reference list is included.

*For corrections, additions, comments and criticisms please email carl.wunsch@gmail.com.

[†]1. AER, Inc., 2. Jet Propulsion Laboratory, 3. MIT, 4. U. Texas Austin, 5. U. South Florida, 6. Harvard U., 7. Cambridge Climate Institute, 8. George Mason U.

1 Introduction: The State Estimate

Purpose

One of the central goals of the World Ocean Circulation Experiment (WOCE) was to produce the first truly global time-varying estimate of the circulation over approximately a decade, an estimate that would be useful in defining the major climatologically important ocean elements. The Estimating the Circulation and Climate of the Ocean (ECCO) project was formed near the start of the WOCE field program so as to address this goal using both the conventional and newly-deploying WOCE observation system, along with the rapidly advancing general circulation modelling capability (Stammer et al., 2002). In this paper, and in subsequent Parts, this WOCE goal is addressed by defining a time-dependent climatology over the 20-year (bidecadal) interval 1994-2013. Little or no dynamical or kinematical interpretation is provided—that is left to other authors and times.

Various oceanic climatologies are in use by the oceanographic and climate dynamics communities. They serve as tests of models, as initial conditions, and as a basic descriptor of the ocean. Definitions of climatologies vary widely both in terms of how they were formed and the durations they represent. Here we describe a 20-year average modern climatology from a dynamically consistent model that also has a consistent fit to the majority of global data between 1992 and 2015 (Wunsch and Heimbach, 2013). The climatology is based upon the ECCO version 4 state estimate (Forget et al., 2015). It derives from a least-squares fit of the MITgcm (Marshall et al., 1997; Adcroft et al., 2004; Forget et al., 2015) to the numerous and diverse global observations. A summary would be that all of the Argo, altimetry, the CTD hydrography appearing in the WOCE Climatology and successors (Gouretski and Koltermann, 2004; Talley et al., 2016), all extant, bias error-corrected XBTs, the considerable elephant seal profile data (Roquet et al., 2013), GRACE mission mean and time-dependent geoids, satellite-measured sea surface temperature and salinity, and the ECMWF¹ ERA-interim reanalysis of the meteorological variables (Dee et al., 2014), have been included, with the fits inferred to be adequate relative to the estimated uncertainties of the data. (Atmospheric reanalyses should not be considered “data”, however.)

Previous climatologies, e.g. Levitus et al. (1982) and its later incarnations as the NOAA World Ocean Atlas, or Gouretski and Koltermann (2004) have usually been based only upon temperature and salinity averages and over much longer time intervals than employed here. Other climatologies (e.g., AchutaRao et al., 2007) have focussed on the upper 700 or 1000m and relied heavily on XBT measurements. As such, all these suffer from the very great inhomogeneities

¹European Centre for Medium Range Weather Forecasts

59 of data distribution prior to the WOCE period and a series of untestable statistical hypothe-
60 ses (see e.g., Wunsch, 2016; Boyer et al., 2016). This present climatology differs from earlier
61 ones most obviously in its production of the three-dimensional, time-varying, three components
62 of velocity and of a self-consistent surface meteorology, as determined at the model time-step,
63 $\Delta t \approx 1$ h. Use of *any* fluid climatology confronts one basic problem: that the resulting time or
64 space-time average fields do not satisfy any simply derivable equations of motion—requiring a
65 variety of turbulence closure schemes—and the relationships among the different variables can
66 be complicated and poorly known. Here, time/space means of fluid quantities are based upon
67 the uniform average of fields exactly satisfying the model equations at each model time-step
68 (nominally 1 hour) and grid-point. Some authors have used ocean general circulation models fit
69 to data in methods analogous to those in meteorology and commonly known as “reanalyses.”
70 These, unfortunately, are usually not property conserving (heat, salt, momentum, etc.) and
71 thus unsuitable for global-scale climate calculations (see e.g., Wunsch and Heimbach, 2013; and
72 Fig. 1 of Stammer et al., 2016).

73 A number of sketches of global scale analyses of earlier multi-decadal ECCO estimates has
74 been published starting with Stammer et al. (2002). An earlier 16-year global time-average was
75 described by Wunsch (2011), with a focus on the accuracy of Sverdrup balance, and Wunsch and
76 Heimbach (2014) discussed the heat content changes. Liang et al. (2016a,b) describe the vertical
77 redistribution of heat. In general, the present solution differs only subtly from those previously
78 used, with the chief differences being ascribed to the inclusion of more data over a longer
79 duration, inclusion of geothermal heating, improvements in the handling of sea ice, and where
80 appropriate separate uncertainties for time-average and time-anomaly measurements. Solutions
81 are generally robust, as the great volume of ocean in the model state vector is in near-geostrophic
82 balance with the density field at all times longer than a few days.

83 By choosing the period following 1994, a much more nearly uniform global data coverage
84 is obtained than was possible earlier. Chief among the remaining data inhomogeneities are the
85 intensification of the Argo float profile data availability after about 2005.

86 Any temporally averaged state will be considerably smoother than states which are sampled
87 more or less as “snapshots.” Thus classical hydrographic sections (e.g., Fuglister, 1960 or the
88 various WOCE Atlases) show many small-scale features which vanish on averaging. Suppressed
89 features include internal waves, tides, and geostrophically balanced eddy motions. Meandering
90 currents, such as the off-shore Gulf Stream, are broader and smoother than in any near-synoptic
91 estimate. In addition, fluid regions that are only marginally or poorly resolved numerically
92 (particularly boundary currents), will be smoother than even a true 20-year average would be.

93 No model with a nominal horizontal grid-spacing of 1° of longitude can resolve small-scale

94 circulation features, which include the important boundary currents. Nonetheless, the near-
95 geostrophy of the bulk of the ocean supports the conjecture that to the extent that a successful
96 fit to the interior temperature, salinity, and altimetric fields and surface boundary conditions, has
97 been obtained, the boundary currents will be forced by the interior flows to carry the appropriate
98 amount of mass (volume), temperature, etc. so as to satisfy the basic overall conservation laws.
99 This conjecture, upon which we rely, can be regarded as a formal statement of that used by
100 Stommel and Arons (1960) in their discussion of deep boundary currents—whose existence and
101 structure was fixed by the mass and property requirements of the interior flow—even though
102 they were not dynamically resolved.

103 As with any estimation problem, a crucial element in the determination of the best values
104 lies with the use of realistic error estimates for *all* of the data that are being fit. For a full
105 discussion of the error estimate used here, reference must be made to the literature. Temperature
106 measurements are described by Forget and Wunsch (2007) and Abraham et al. (2013). Altimetry
107 accuracies are discussed by Fu and Haines (2013) and Forget and Ponte (2015). For the gravity
108 data from the GRACE mission, see Quinn and Ponte (2008). Satellite surface salinities are
109 addressed by Vinogradova et al. (2014). Meteorological variable accuracies are described e.g.,
110 by Chaudhuri et al. (2013).

111 This paper is *not* an in-depth analysis of *any* features of the global ocean circulation. It
112 is instead mainly visually descriptive—a suggestive pictorial subsample—intended primarily to
113 serve as an invitation to the wider community to exploit it by demonstrating various products.
114 With the widespread recognition that a steady-state ocean never exists, attention turns instead
115 to the temporal changes over the estimation period.² Here for descriptive purposes, some pictures
116 of changes year-by-year for 20 years, by 20-year averages by month, and by season are displayed.
117 All results can readily be calculated month-by-month at the expense of using a larger volume of
118 numbers.

119 Most results are intended mainly to be indicative of possibilities rather than being the most
120 precise or accurate possible. Thus for example, the heat capacity, c_p and the mean density, $\bar{\rho}$
121 are treated as constant in calculations of heat uptake even though both are (weak) functions of
122 position.

123 *The State Estimate*

124 The ECCO state estimate is obtained from the *freely-running* MITgcm after the adjustment
125 of the control parameters required to fit the data. In the least-squares methodology with La-
126 grange multipliers (see Wunsch and Heimbach, 2013), the entire interval 1992-2015 has been

²Forget (2010) presented an 18-month estimate from an earlier ECCO state estimate, and which is closer to being a “snapshot” rather than a climatology.

127 fit to the data. Parameters adjusted include the three-dimensional, top-to-bottom, initial con-
128 ditions, internal mixing coefficients, and the surface meteorology. At any given time in the
129 estimation interval, the solution represents data both preceding and *following* that date so that
130 the equations are always satisfied while coming as close to the data as possible within uncertainty
131 estimates. The 20-year period 1994-2013 has been chosen for averaging as sufficiently distant
132 from the poorly constrained earlier years before the high accuracy altimetry begins in late 1992
133 and the time of the then non-existent data following 2016. The period corresponds to that of
134 complete coverage by satellite altimetry, the WOCE CTD survey, and the interval after about
135 2005 when the Argo array became fully-deployed. All data, plus the ECMWF estimate, have
136 been assigned uncertainties that include both instrumental and natural noise. After adjustment
137 of the parameters, the free-running forward model satisfies all basic conservation requirements
138 and is structurally no different from any other unconstrained model estimate.

139 No state estimate is definitive or “correct”; they are “best-estimates” for the present time:
140 data are continuously added, both from more recent years and previously omitted earlier val-
141 ues; estimated data errors are sometimes revised; models are improved; and in all situations,
142 minimizing iterations are ongoing. Values shown here are obtained from ECCO version 4 as of
143 mid-November 2016.

144 Undoubtedly the state estimate has residual systematic errors at some level, particularly
145 in data-poor regions and times. To some extent, these will be removed when considering only
146 temporal changes in the state over the 20-years and these latter are given some emphasis.
147 Uncertainty estimates remain an amorphous problem: much of the variability in the model
148 represents deterministically evolving elements. Stochastic elements are introduced by weather,
149 some longer-period meteorological variability, and by elements of the initial-conditions best
150 regarded as random. Because the true probability distributions are not known, discussion of
151 estimate uncertainties is postponed to Part 4.

152 A full description of the many features of a 20-year average global ocean circulation requires
153 a book-length publication, if not a library. The strategy here is to sketch the gross hydrographic
154 and circulation features and to do a limited comparison to a few of the special regions (bound-
155 ary currents, mixed-layer, etc.) to provide some of the flavor of the differences between an
156 average and both the more common limited-time analyses usually available (classical synoptic
157 hydrographic sections) as well as the far more inhomogeneous published climatologies.

158 With time-mean fields being spatially and temporally smoother than in nominally synoptic
159 measurements, second order quantities such as the time averages e.g., $\langle \mathbf{v} \rangle \langle T \rangle \neq \langle \mathbf{v}T \rangle$, where $\langle \cdot \rangle$
160 denotes a space-time average, and the difference may be very large. Much of physical oceanogra-
161 phy has been based upon the unstated assumption that quasi-synoptic measurements represented

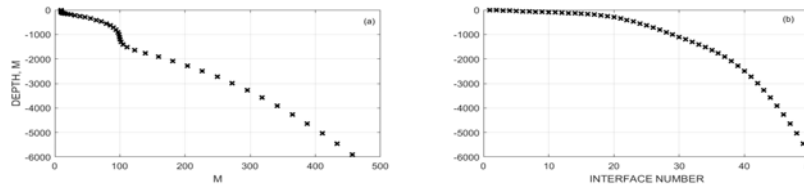


Figure 1: (a) Level thicknesses; (b) level depths in the ECCO version 4 of the MITgcm.

{interfaces_la

162 the mean motion. Thus e.g., the calculation of Sverdrup balance, or of “abyssal recipes”, are
 163 implicitly steady-state results, despite the common use of individual hydrographic sections. Here
 164 true 20-year average estimates are now possible. This description and discussion thus largely
 165 focusses on the properties of single variables, T, u , etc., their 20-year means and estimates of
 166 the deviation from those means. As Part 1, this paper is confined to the hydrographic products,
 167 T, S and their implications for surface elevation, mixed layer depth, deformation radii, etc. The
 168 velocity field and its property transports are discussed in Part 2. Most emphasis is placed on the
 169 global fields. A number of higher resolution, regional versions, of the state estimate exist (e.g.,
 170 Gebbie et al., 2006; Mazloff et al., 2010), and a high northern latitude version is forthcoming
 171 (An Nguyen, personal communication, 2016), but these are not further discussed here.

172 All of the ECCO system output described here is available in Matlab form at: [http://mit.ecco-](http://mit.ecco-group.org/opendap/diana/h8_i48/contents.html)
 173 [group.org/opendap/diana/h8_i48/contents.html](http://mit.ecco-group.org/opendap/diana/h8_i48/contents.html)³ as 20-year means, 20-separate annual means,
 174 20-year average individual months, and 20-year average seasonal means (DJF, MAM, JJA, SON)
 175 on a grid in 50 vertical levels, of thickness plotted in Fig. 1. Many studies are best done in
 176 isopycnal-like coordinate systems; but the present description is confined to calculations in geo-
 177 metrical (latitude-longitude-depth) coordinates, with the interpolations to isopycnals postponed
 178 (but see Speer and Forget, 2013 for a mode water discussion).

179 2 Temperature Field

180 *Data Misfits*

181 Figs. 3-4 show the misfit to the mean temperature over 20 years at two different levels.⁴

³Or contact Carl Wunsch directly (cwunsch@mit.edu) for data or advice.

⁴The projections used here are the so-calledloximuthal, with the Atlantic placed close to the center. The rationale is that this form both avoids the visual dominance of the tropical Pacific—which tends to get excess attention—and shows the Arctic as a reasonable fraction of the total. Color scales mostly follow the advice of Thyng et al. (2016) as both most suitable for colorblind individuals and with the least visual distortion of the

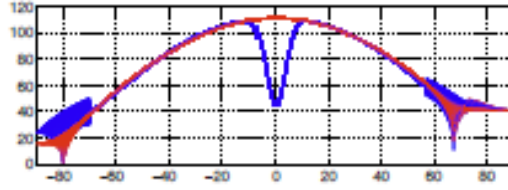


Figure 2: Latitude (blue curve) and longitude spacing in kilometers as a function of latitude (from Forget et al., 2015). Higher latitude spacing exists near the equator. At high latitudes the more complex grid leads to a distribution of spacings (see Figs. 1,2 of Forget et al., 2015). Most of the high latitude southern region is land.

{forget_etal_f

182 Values are calculated from point values where available and then gridded. Although some
 183 systematic misfits do appear, particularly in the region of the unresolved western boundary
 184 currents and near-surface in the tropical oceans, the bulk of the system is within a fraction of a
 185 degree of the observed averages. Although not shown here, misfits can be readily computed for
 186 each year, each season, and each month if desired. In an ideal world, the misfit values should
 187 be Gaussian, here roughly consistent with the displayed histograms.

188 The implications of regional misfits to observations is a problem generic to the use of *any*
 189 general circulation model: if a model fails to adequately mimic the observations in a particular
 190 place at a particular time, does that render useless the solution in other regions and times?
 191 The existence of the adjoint (dual) solution as part of the state estimate permits, in the present
 192 situation, an answer in terms of global sensitivities computed from the dual (e.g., Heimbach et
 193 al., 2011). That discussion is postponed to Part 3 of this climatology.

194 *Estimated Solutions*

195 A representative set of horizontal charts and vertical sections is displayed here. For temper-
 196 ature, the charts and sections are oceanographically qualitatively consistent with conventional
 197 descriptions of the large-scale, averaged oceanic circulation. Thus for example, the 20 year av-
 198 erage temperatures at 5 and 105m in Figs. 5, 6 show all of the conventional near-surface gyres,
 199 the strong Southern Ocean thermal fronts, the upwelling regions off Africa, California and South
 200 America, as well as numerous other expected features. The differences between these two maps
 201 are a rough measure of the mixed layer temperature gradient (discussed below). Some mapped
 202 values are shown with a histogram of their distribution; where not shown they are typically
 203 Gaussian—or at least unimodal. Most property anomalies are strongly unimodal; time average

fields.

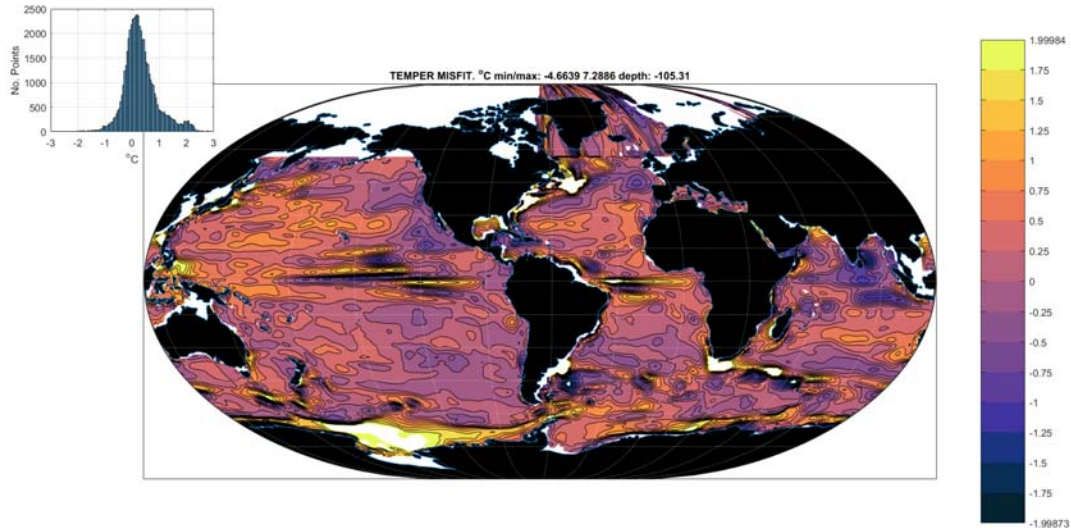


Figure 3: Misfit to the 20-year average temperature (°C) at 105m including Argo, XBT, CTD, and elephant seal profile data. Inset shows a histogram of values. A small number of outliers here and in other charts have been suppressed.

{misfit_temper

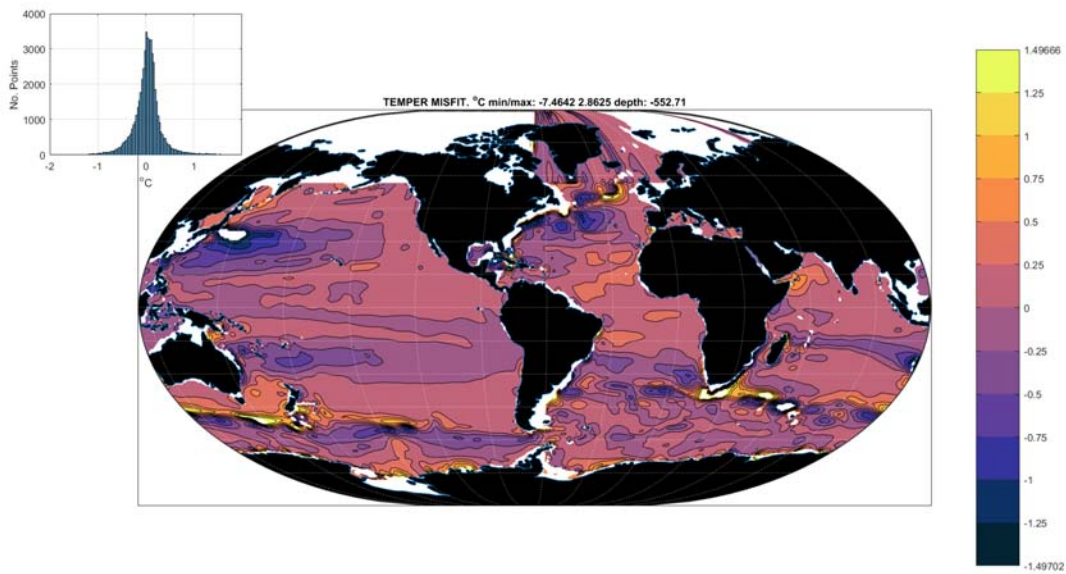


Figure 4: Same as Fig. 3 except at 553 m.

{misfit_temper

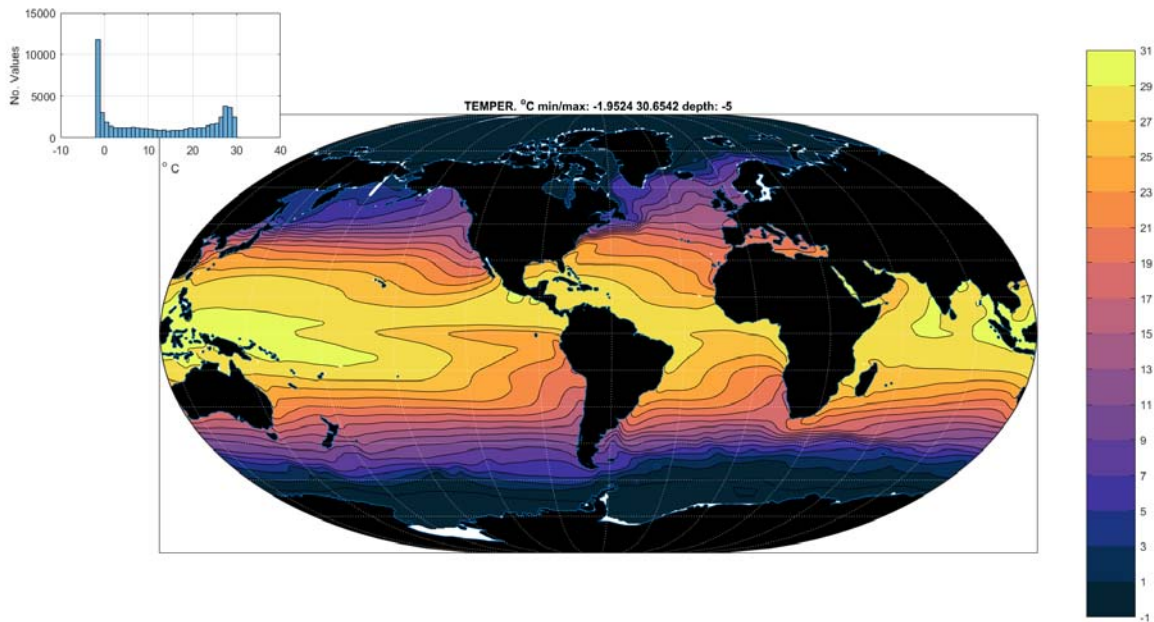


Figure 5: Twenty-year mean potential temperature at 5m depth ($^{\circ}\text{C}$). Inset shows the histogram of values.

{temperature_2

204 properties usually are not. An example of the deep temperatures is shown in Fig. 7 near 2100m
 205 depth.

206 At 2100m (Fig. 7) the Atlantic Ocean warmth relative to the rest of the world is obvious,
 207 as is the large-scale thermal gradients extending away from the Southern Ocean.

208 A few traditional potential temperature sections are shown in Figs. 8-11. As compared to
 209 standard atlas sections (e.g., the WOCE Atlas Series) they display, as expected, similar large-
 210 scale features, but tend to be considerably smoother. Nonetheless, a number of small scale
 211 features survive the 20-year averaging, particularly in the Southern Ocean (Fig. 10).

212 *Global Mean temperatures:*

213 The 20-year mean temperatures of the global ocean, including the full Arctic, are shown in
 214 Table 1. Volume-weighted global average temperature is 3.32°C as compared to Worthington's
 215 (1981) estimate of 3.51°C , but who had no Arctic and very few Southern Ocean values (see
 216 his Fig. 2.1 and Fig. 10 here). Table 1 lists volume-weighted mean temperatures, while the
 217 ad hoc standard errors are the raw standard deviation of the unweighted temperatures and
 218 salinities from the spatial variations of the 20-year means. They give a rough idea of the range
 219 of temperatures (and salinities) that enter. On the other hand, the standard errors of the

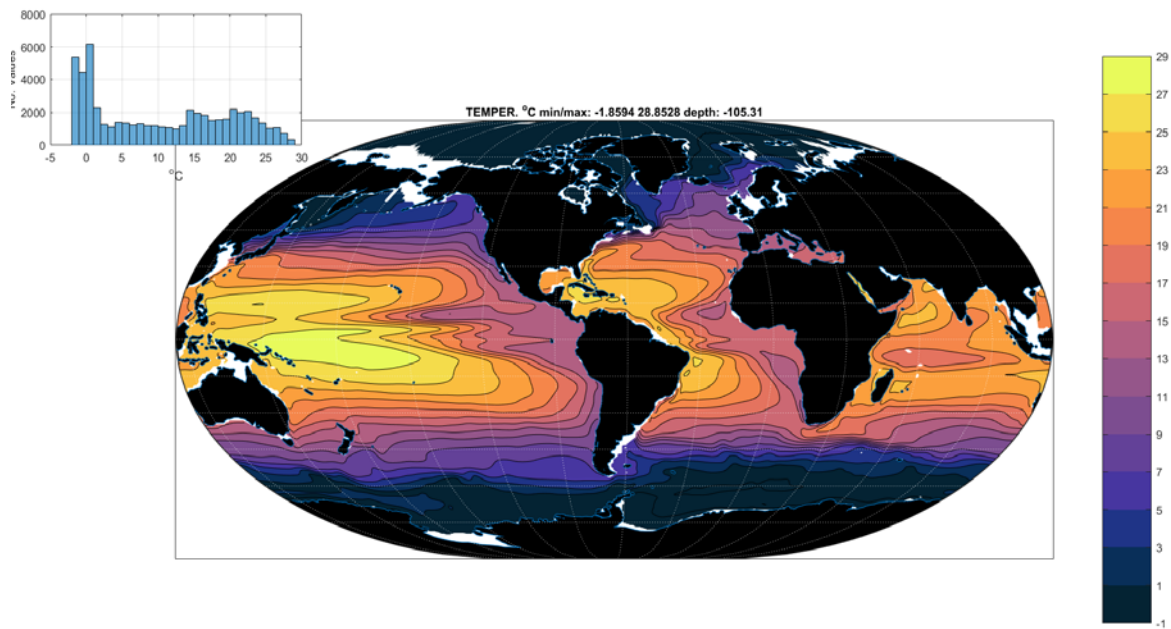


Figure 6: Twenty-year average potential temperature at 105m (°C). Note change in scale from Fig. 5.

{temperature_2

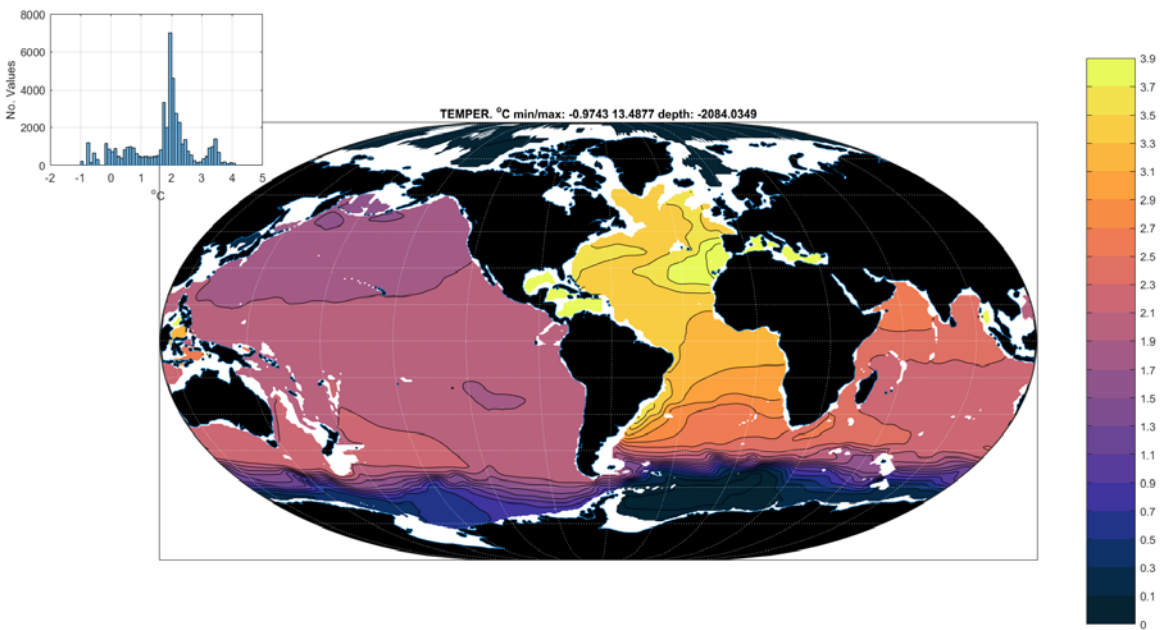


Figure 7: Twenty-year average temperature at 2084m (°C). Color saturates at 3.9 °C with the maximum approaching 13.5°C in the Mediterranean and Gulf of Mexico.

{temperature_2

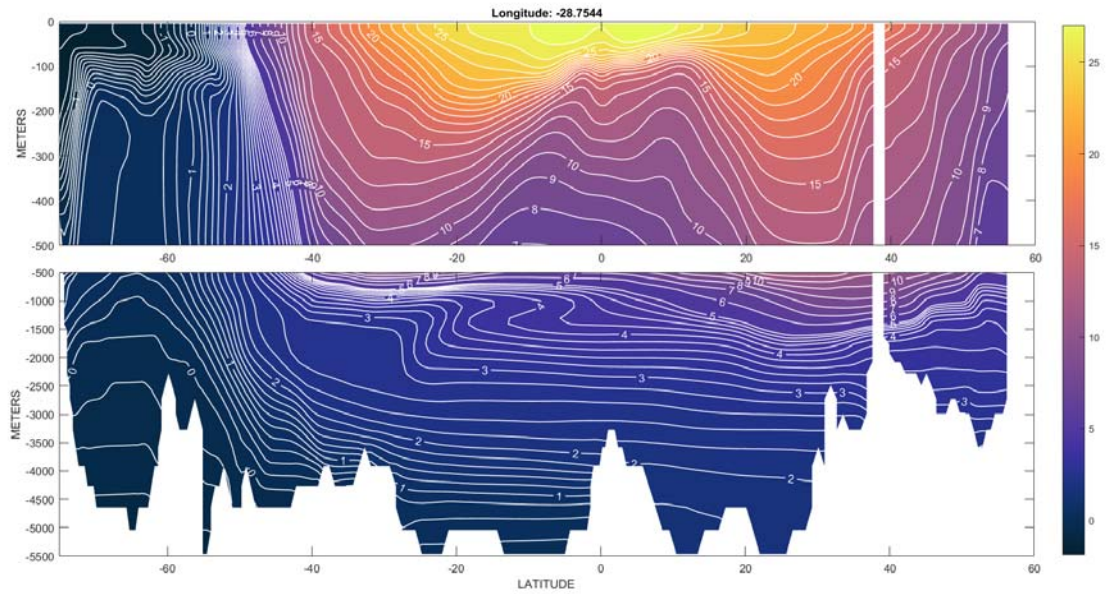


Figure 8: Twenty-year mean section ($^{\circ}\text{C}$) of potential temperature down 28.8°W in the Atlantic ocean. {temp_20yearme

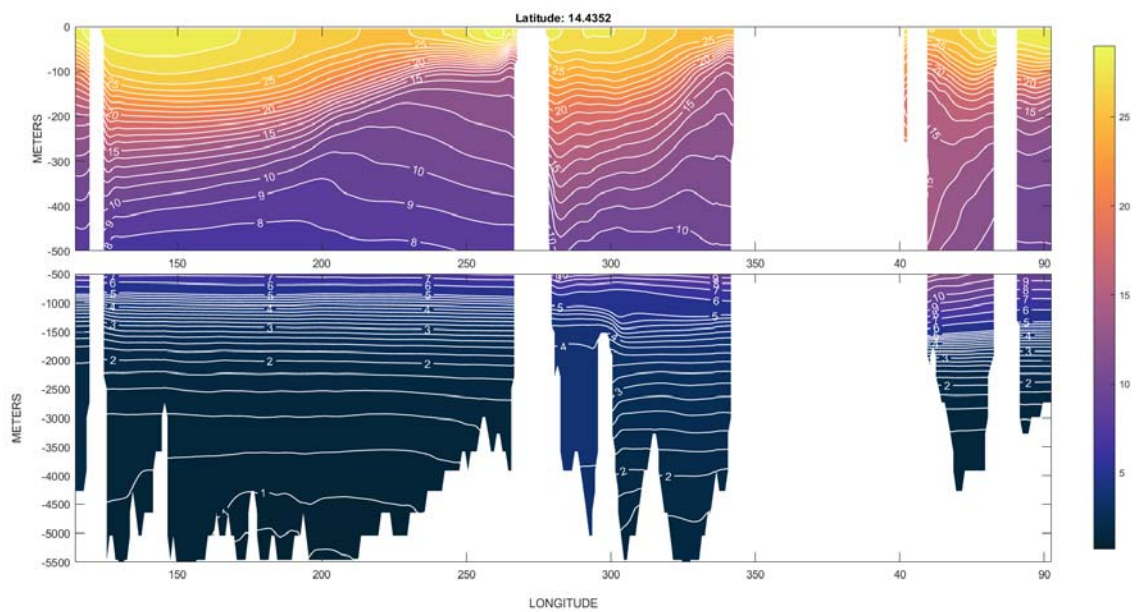


Figure 9: Twenty-year mean potential temperature in all three oceans along 14°N . {temp_20yearme

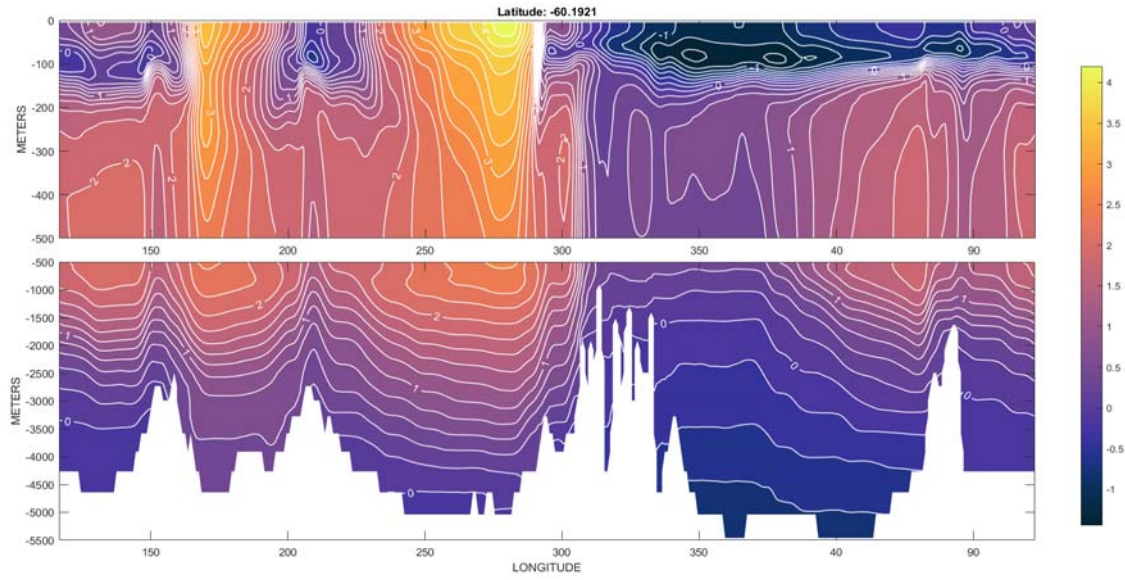


Figure 10: The twenty-year average temperature along 60°S through the Drake Passage.

{temp_20yearme

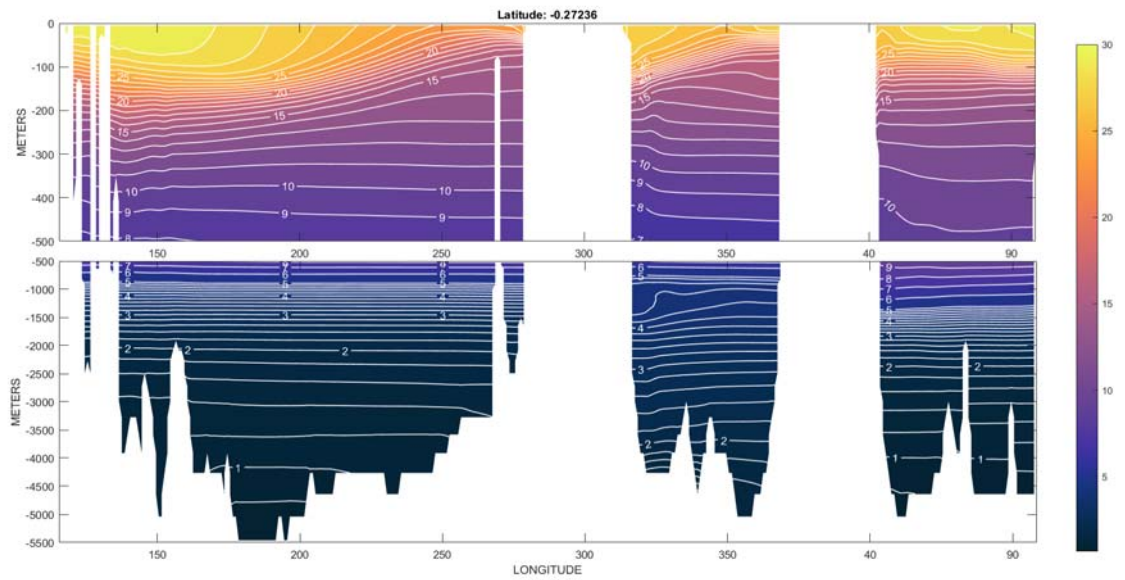


Figure 11: Equatorial 20-year mean potential temperature section.

{temp_20yearme

Depth Range (m)	Mass (Zetta (10^{21}) kg)	Mean Temperature, °C	Mean Salinity, o/oo
0-100	0.04	15.4(9.3)	34.74(0.10)
0-700	0.32	9.1(7.4)	34.74(0.10)
0-2000	0.90	5.2(6.4)	34.70(0.07)
0-3600	1.5	3.8(6.0)	34.72(0.06)
3600 to bottom	0.31	0.9(0.34)	34.73(0.003)
0 to bottom	1.7	3.32(6.7)	34.72(0.06)

Table 1: Mean temperatures and salinities over 20 years as integrated to various depths. Parenthetical values are the standard deviation of the annual mean temperatures and salinities going into the calculation. They are not any sort of standard error. Standard deviations of volume weighted temperatures are far smaller (e.g., 2×10^{-5} degree C). A constant density of 1029 kg/m^3 was used in computing the total masses for each depth range, and which are also displayed.

{table_vols}

fractional volume weighted temperatures are far smaller: e.g. for the global mean temperature, that standard error is $4 \times 10^{-7} \text{ }^\circ\text{C}$, but which is in large part a measure of the volumetric variability assigned to each temperature under the pretence of statistical independence of each value. Let V_{ijk} indicate the volume occupied by any grid box, at horizontal location indices i, j , and with depth index k . Fig. 12 shows the distribution of fractional values $T_{ijk}V_{ijk}/\sum_{ijk} V_{ijk}$ in the 20-year mean temperatures. There the vertical index k ranges over the top 100m, and over the full water column. The bimodal, non-normal distribution renders an ordinary variance estimate of the mean not particularly meaningful. Useful uncertainties would come from computing means from resampling strategies dictated by actual observational distributions (e.g., Wunsch, 2016; Boyer et al., 2016), but which is not carried out here. Such estimates depend sensitively on statistical assumptions about the space-time distribution for “infilling” purposes.

2.1 Annual Changes

Figs. 13-16 show individual year-long average anomalies relative to the 20-year average at two representative depths. Apart from major regional features (e.g., the Gulf of Alaska and the Indo-Pacific tropics), these results emphasize the very intricate patterns appearing, and the consequent highly challenging space/time sampling program for forming large-spatial scale means.

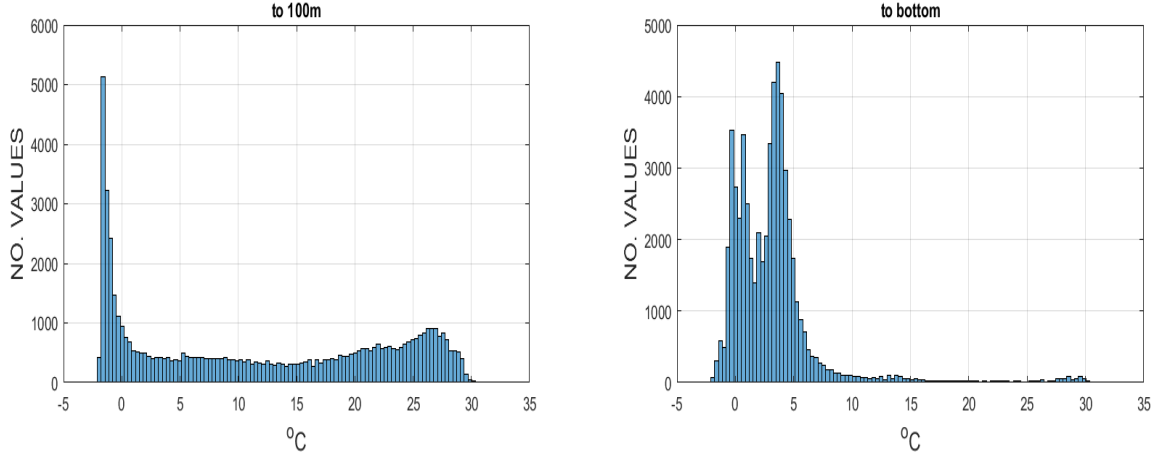


Figure 12: (Left panel). Histogram of volume weighted temperature values of $T_{ijk}V_{ijk}/\sum_{ijk}V_{ijk}$ for the global 20-year temperature mean in the top 100m of the model. (Right panel) Same as the left panel except for the entire water column. ijk are the three grid box indices, V_{ijk} is the volume assigned to temperature T_{ijk} . Note the bimodal nature of the distributions and the long-tail for the top 100m values. See also, Fig. 5.

{temp_20yrmean}

Period & Fraction of Water Column	1 W/m ² Heating/Cooling Rate	1 mm/y GMSL Change
1 Year, Full Depth	0.002°C	0.0015°C
20 Years, Full Depth	0.04°C	0.03°C
1 Year, Upper 700 m	0.01°C	0.008°C
20 Years, Upper 700 m	0.2°C	0.16°C
1 Year, Below 700 m	0.0025°C	0.002°C
20 Years, Below 700 m	0.05°C	0.04°C

Table 2: Approximate oceanic temperature changes implied by a 1 W/m² heating (or cooling)-rate over different times and depths, as well as the temperature change equivalent of a 1 mm/y global mean sea level (GMSL) change. For rough calculation purposes, the heat capacity $c_p = 4000\text{J/kg/}^\circ\text{C}$, $h = 3800\text{m}$, $\rho = 1029\text{kg/m}^3$, Expansion coefficients α are in the range $5 - 30 \times 10^{-5}/^\circ\text{C}$ (Thorpe, 2005) and smaller near the freezing point. Modified from Wunsch and Heimbach (2014).

{table2}

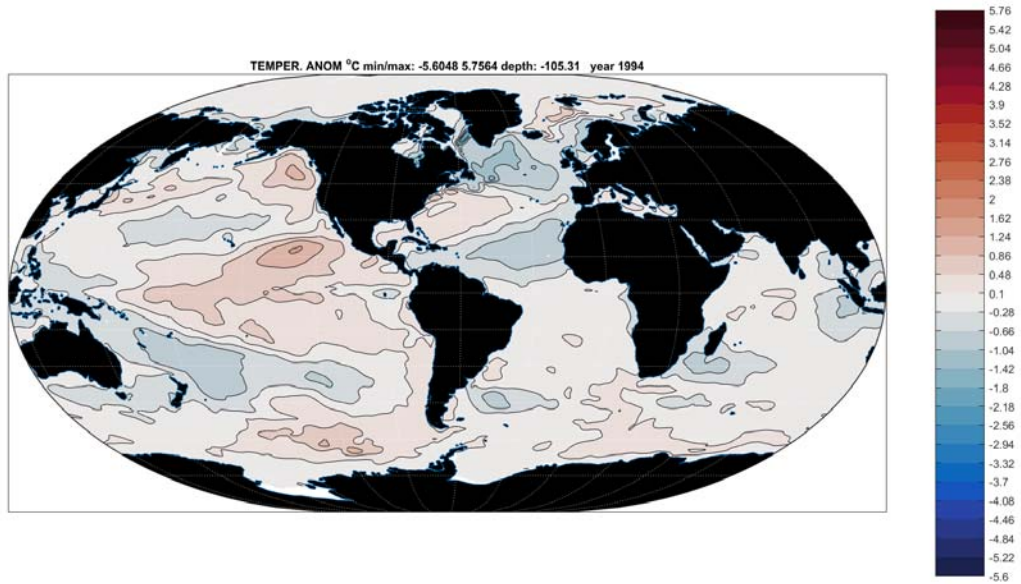


Figure 13: Anomaly of temperature in 1994 relative to the 20 year mean at 105m.

{temp_anom_199

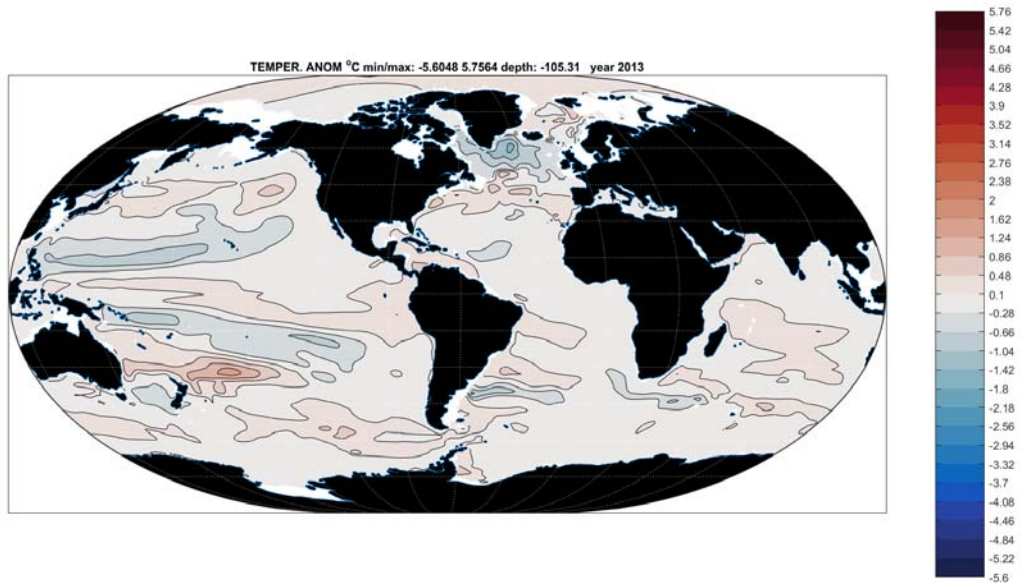


Figure 14: Twenty-year mean anomaly of temperature at 105m in 2013, twenty-years after that in Fig. 13.

{temp_anom_201

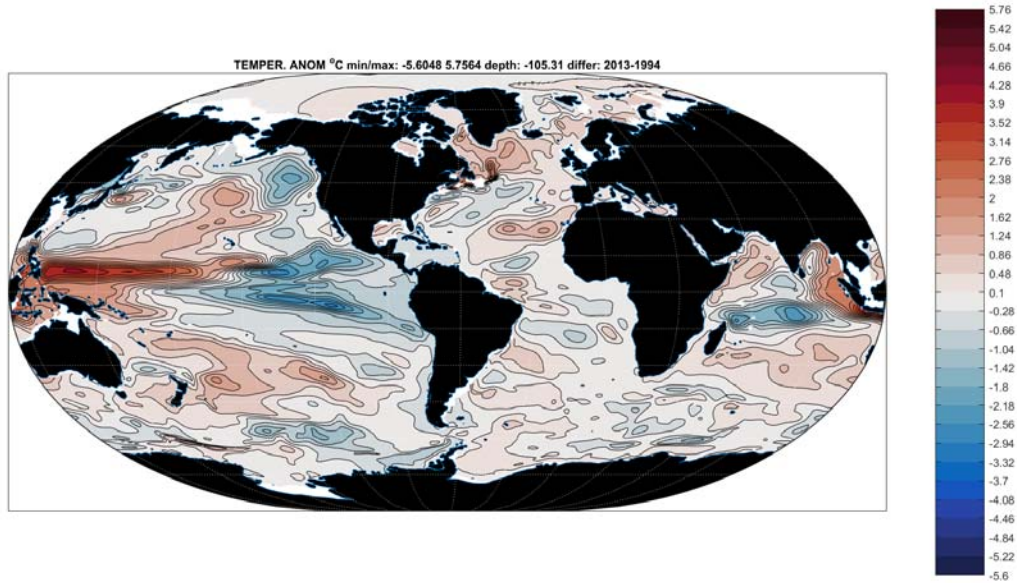


Figure 15: Change in temperature between 2013 and 1994 at 105m, the difference of Figs. 14 and 13.

{temp_anom_201}

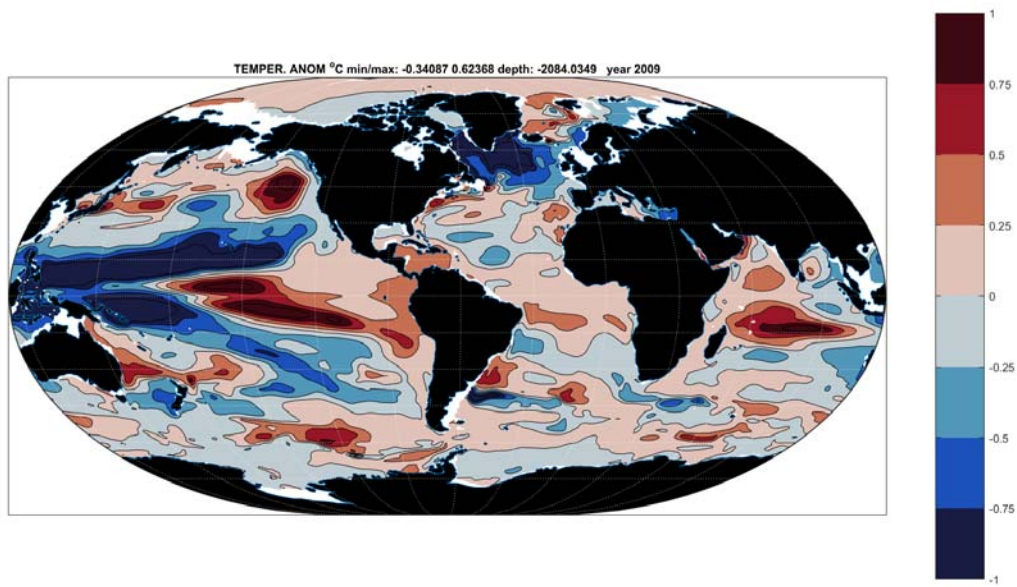


Figure 16: Temperature anomaly at 2100m in 1994 relative to the 20-year mean.

{temp_anom_200}

237 2.2 Heat Uptake

238 A large literature has grown up surrounding the notion of a “hiatus” in global warming during
239 the nominal period 1998-2013. No consensus has emerged over the reality or significance of this
240 phenomenon in the presence of very noisy, under-sampled sets of data as well as the exchanges
241 (re-arrangements) of heat energy *within* the ocean itself. To the extent that the phenomenon is
242 a real one, it has been argued that the ocean uptake of heat must have increased during that
243 period, subject to the assumption of little or no change of net solar radiation during that interval.
244 Conversion of out-of-equilibrium heating rates, which are minute compared to the background
245 values, is not very intuitive. Thus Table 2 converts a net ocean uptake change of $1\text{W}/\text{m}^2$ into
246 an approximate temperature change, depending upon the depth over which the change is to be
247 attributed. So for example, if the changed heat content all resides in the upper 700m, the mean
248 temperature would change by 0.2°C in 20 years. Similarly, the Table also shows the temperature
249 change over different layers that would lead to a $1\text{mm}/\text{y}$ change in global mean sea level. In
250 terms of the ordinary, measured, oceanic temperature, the changes are dauntingly small.

251 The inferred 20-year change in heat content is depicted in Fig. 17, displaying the computed
252 yearly-average global mean temperature anomaly for each year. Deeper values are accompanied
253 by a least-squares fitting straight-line. The “abyssal” region, 3600m to the bottom shows a
254 slight cooling. Heat content changes, involving the massive volumes in the deeper integrals, are
255 tabulated in Table 3. A map of the vertically integrated heat content can be seen in Wunsch
256 (2016) and see Liang et al. (2016a,b) for further discussion. Negative values in the abyss are
257 most easily interpreted as owing to cooling there during the adjustment from the estimated
258 initial conditions. Discussion of the linear fits and their statistical significance, if any, is left to
259 the references except to say that no obvious evidence of a “hiatus” or other time-limited shift,
260 appears.

261 The global mean ocean temperature shows an increase over 20 years to 2000m of 0.02°C
262 (difference of first and last years and not a fitted trend). That change translates (Table 2)
263 into a heating rate of $0.3\text{W}/\text{m}^2$. The change to 700 m is 0.08°C translating into $0.13\text{W}/\text{m}^2$ not
264 inconsistent with numerous published estimates, including that of Wunsch and Heimbach (2014)
265 from a previous state estimate. Although the upper 100m displays, as expected, a much larger
266 noisiness, including e.g., the 1997-98 El Niño event, the deeper integrals display no such effect.
267 The calculation of differences tends to remove systematic errors in the ECCO system, but a
268 further quantification is not available. The total warming over 20 years includes the *cooling*
269 below 3600m remarked by Wunsch and Heimbach (2014) which persists even with the inclusion

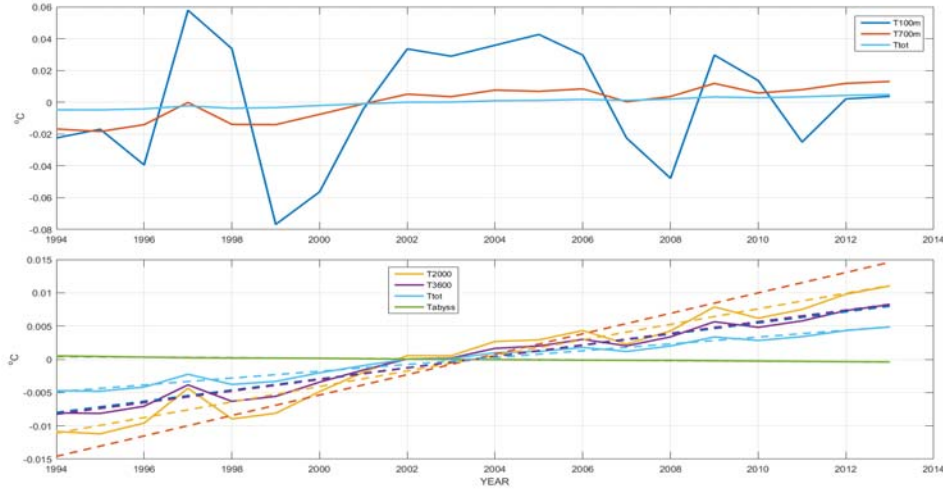


Figure 17: Volume weighted temperature change $^{\circ}\text{C}$ by year. Upper panel is the average to 100m and 700m, and lower panel the averages to 2000m, 3600m, the total top to bottom, and the abyssal layer below 3600m. Dashed lines are a best linear fit using a jackknifed estimate of the uncertainty in the values (not shown).

{heat_content_}

Depth Range (m)	Mean Heat Content (YJ: 10^{24}J)	Temp. Change 20 Yrs $^{\circ}\text{C}$	Warming 20 Year Difference W/m^2
0-100	2.6	0.03	0.02
0-700	11.6	0.03	0.13
0-2000	18.9	0.02	0.26
0-3600	22.2	0.02	0.32
3600-bottom	1.1	-0.09	-0.004
0-bottom	23.3	0.01	0.23

{meanheat}

Table 3: Time-mean heat content in the ocean by depth range in Joules. The net change, converted to W/m^2 , calculated from the difference between 2013 and 1994 is shown. Most of the oceanic mass lies below 700m. Mean temperatures are shown in Table 1.

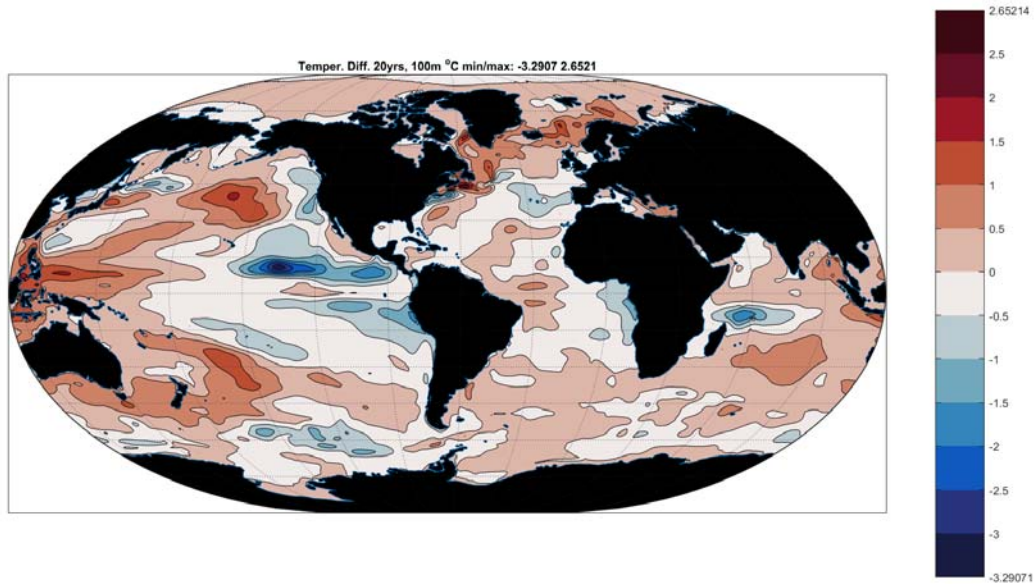


Figure 18: Vertical temperature difference over averaged over the top 100m from 2014-1993. A La Niña pattern is visible, but embedded within a complex structure of global change.

{temp_lastminu

270 of $0.1\text{W}/\text{m}^2$ average geothermal heating⁵.

271 Changes in heat content, as reflected in temperature, have a complex spatial pattern varying
 272 with depth. Figs. 18-20 show the column averaged temperature differences for three represen-
 273 tative depths, including the top-to-bottom. These are presumably the result of interior redistri-
 274 butions, and air-sea fluxes over the 20 years. As always, the irregular sampling distribution for
 275 in situ measurements used alone is challenging if accurate global means are required. Standard
 276 deviations of the annual means, which become part of the discussion of sampling strategies, are
 277 shown in Figs. 21-22 again depicting the strong regionality. Instantaneous standard deviations
 278 are necessarily far larger. Huge standing reservoirs of thermal energy in the ocean, and the very
 279 small dis-equilibrium of the climate system, renders accurate determination of the very slight
 280 reservoir changes to be a difficult problem.

281 **2.3 Annual Cycle**

282 The largest ongoing climatological signal is the seasonal oscillation. Vinogradov et al. (2008)
 283 have described the seasonal cycle of sea level in an earlier ECCO state estimate. Fig. 23-26

⁵More precisely $0.095\text{ W}/\text{m}^2$.

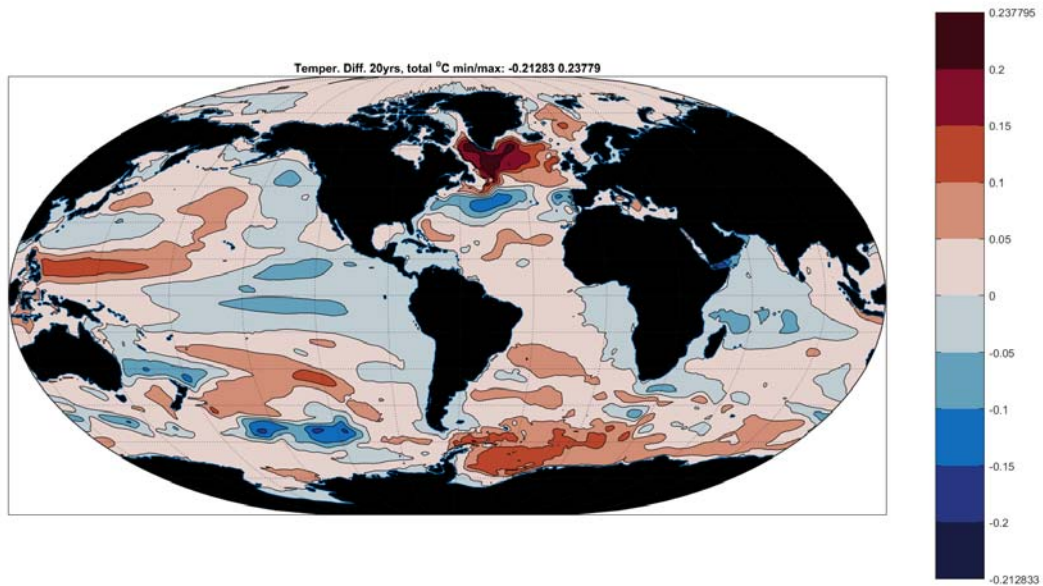


Figure 19: Vertical average temperature change, top-to-bottom, 2013 minus 1994 in °C.

{temp_differen

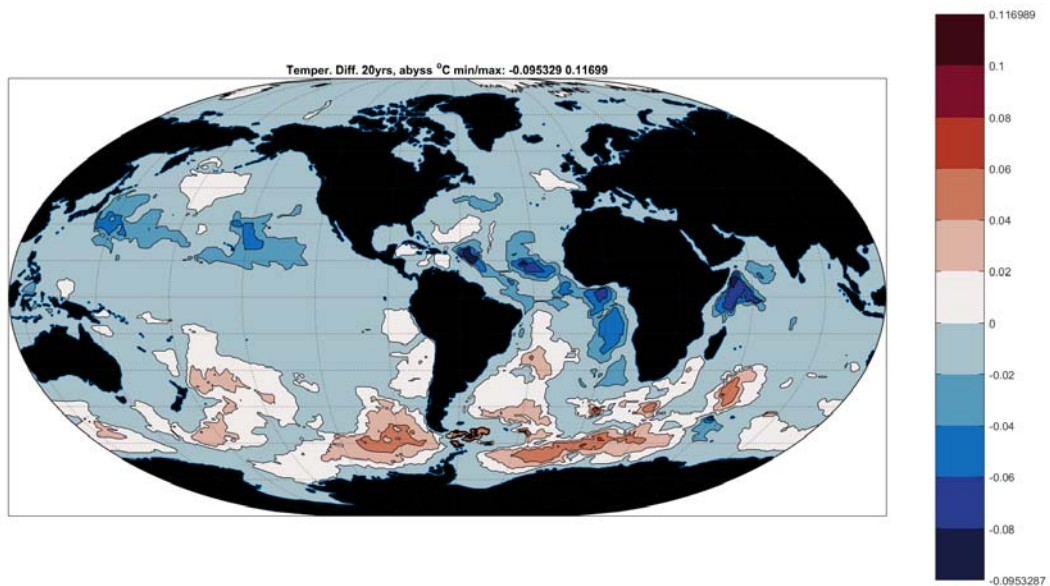


Figure 20: Abyssal temperature change, 3600m to the bottom, over 20 years. The warming of the Antarctic Bottom Water (Purkey and Johnson, 2010) is apparent, with a cooling over much of the rest of the ocean (see Wunsch and Heimbach, 2014).

{temp_lastminu

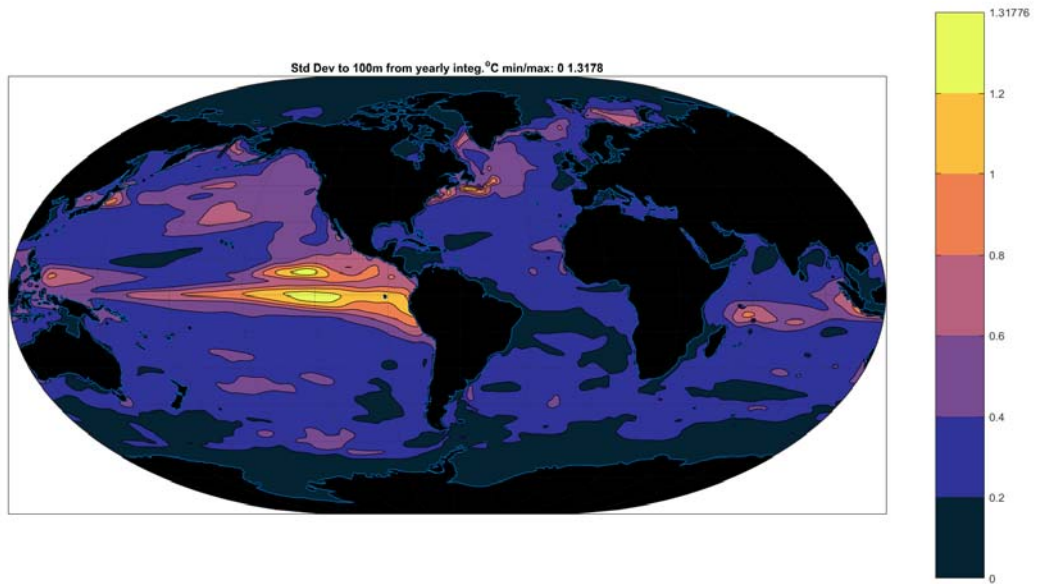


Figure 21: Standard deviation of temperature ($^{\circ}\text{C}$) averaged over top 105m based on yearly variations.

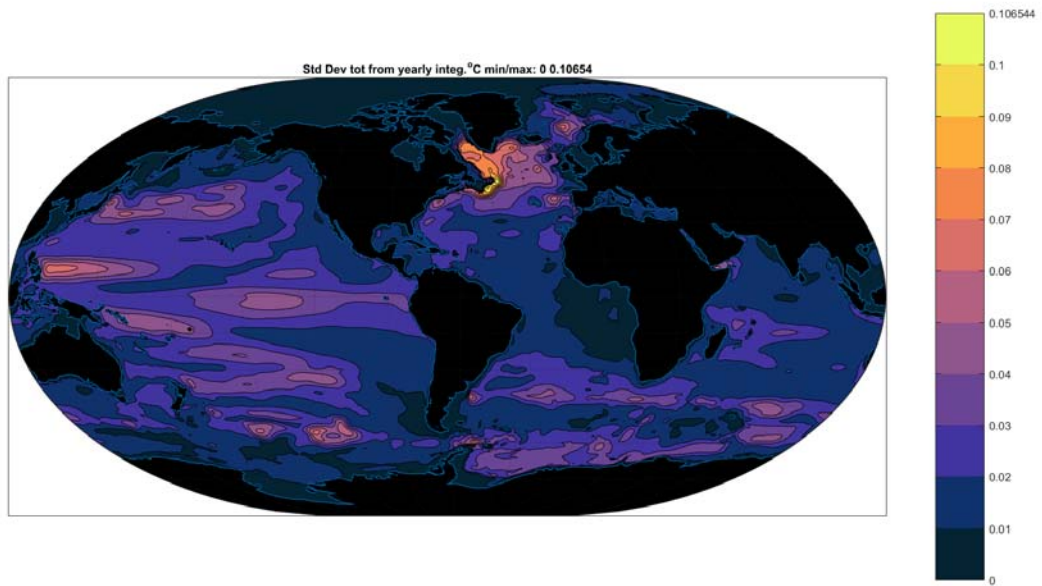


Figure 22: Vertical average temperature, ($^{\circ}\text{C}$) top-to-bottom, standard deviation based on annual fluctuations. Relatively intense values in the northwestern Atlantic Ocean need to be rationalized (some discussion is provided by Hakkinen et al., 2013).

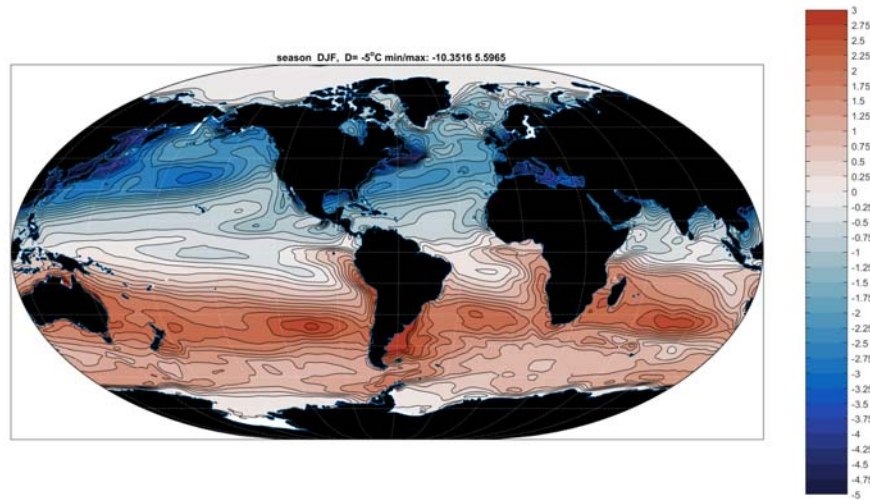


Figure 23: Seasonal (December, January, February, DJF) mean 5m temperature anomalies. The main feature is the interhemispheric anti-symmetry with the conventional larger amplitudes in the northern region.

{temp_djf_5m.t

284 displays the four seasonal temperature anomaly means at the 5m level in the present estimate.
 285 The largest signals are in the shallow regions on the eastern coasts of Asia and North America
 286 where the continental meteorology first encounters the ocean.

287 Non-equatorial vertical propagation of seasonal forcing tends to be suppressed rapidly with
 288 increasing depth (Gill and Niiler, 1973). Some understanding of the overall depth/spatial struc-
 289 ture of the seasonal cycle can be obtained from the singular value decomposition of the seasonal
 290 average temperature. With four seasons, only four pairs of singular vectors fully describe the
 291 patterns, and because the time average of the anomalies vanishes, only three pairs are required.
 292 The singular values are 2706, 1083, 436. Figs. 27-29 show the most energetic component \mathbf{u}_1
 293 for three depths. But from Fig. 30, on the spatial average, the annual cycle in temperature
 294 penetrates only to about 100m, and beneath that depth (in the spatial average) it is negligible.

295 3 Salinity Field

296 *Data Misfits*

297 Twenty-year average salinity misfits are displayed in Figs. 31, 32. Largest values and outliers
 298 are at continental margins where model resolution is inadequate, and where issues concerning
 299 land runoff data accuracies persist.

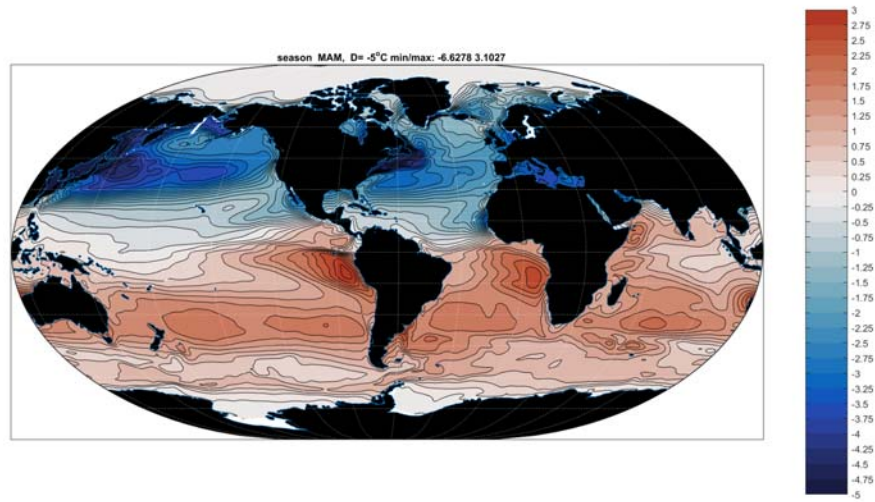


Figure 24: Twenty-year average temperature anomaly March, April, May at 5m.

{temp_mam_5m.t

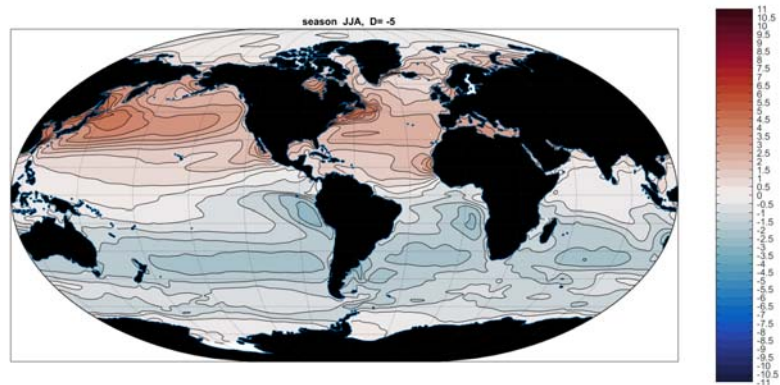


Figure 25: Twenty-year average temperature anomaly at 5 m, June, July, August.

{temp_jja_5m.t

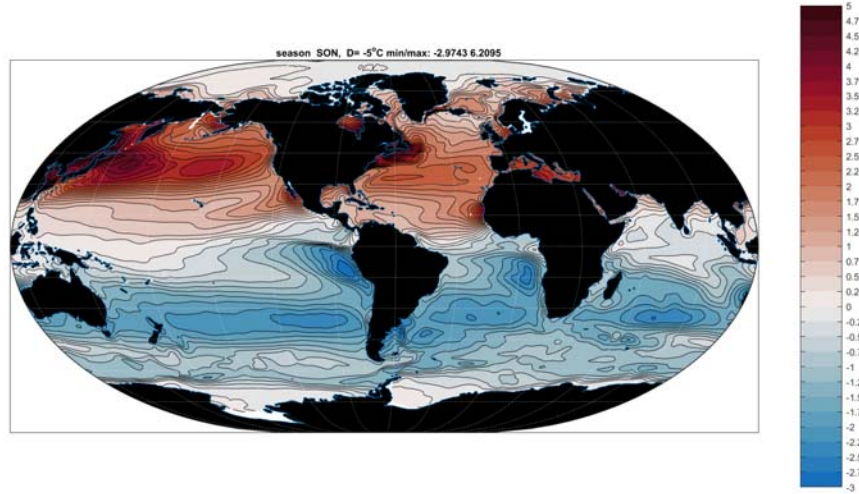


Figure 26: Twenty-year seasonal mean temperature anomaly at 5m September, October, November.

{temp_son_5m.t

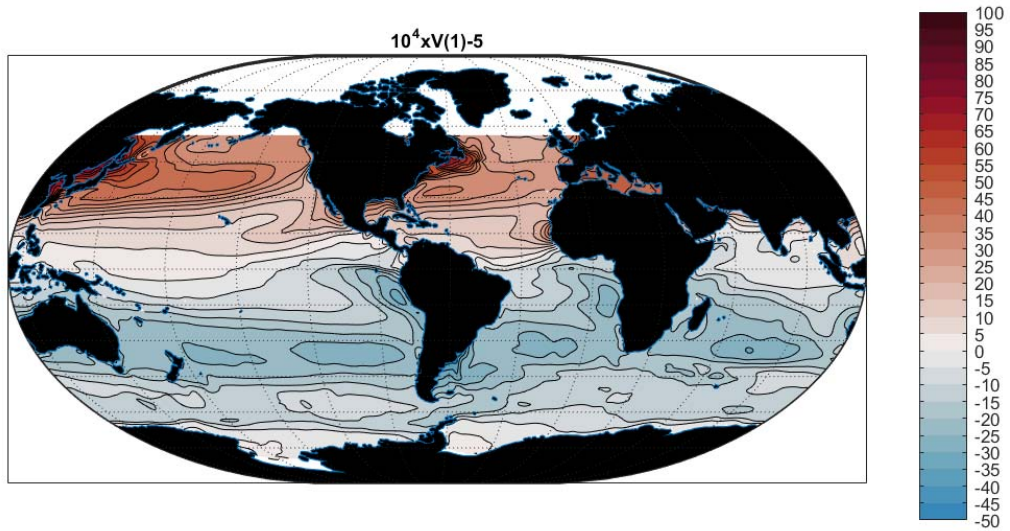


Figure 27: The first EOF (singular vector) of temperature at 5m. multiplied by 10^4 . Values are dimensionless with units being ascribed to the singular values.

{temp_v1svd_5m

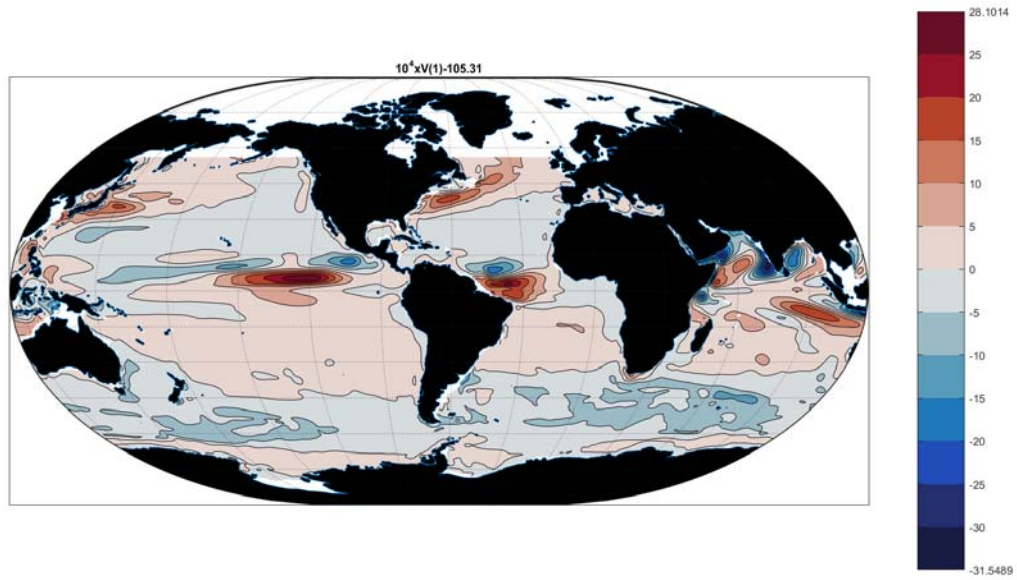


Figure 28: Same as Fig. 27 except at 105m.

{temp_v1svd_10

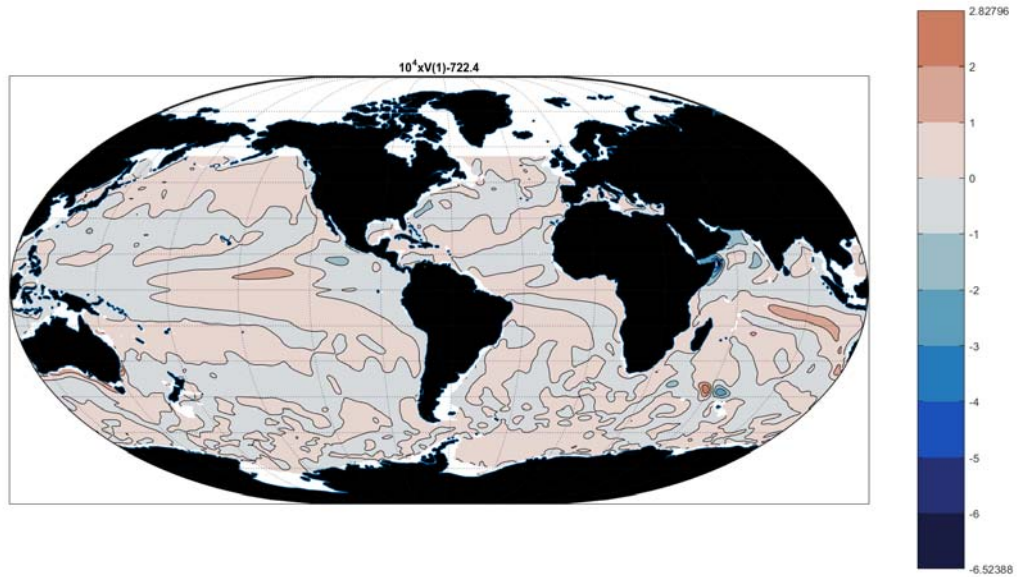


Figure 29: Same as Fig. 27 except at 722m. A monsoonal response is visible, particularly in the eastern and western tropical Indian Ocean. Otherwise, the annual cycle at this depth is effectively negligible.

{temp_v1svd_72

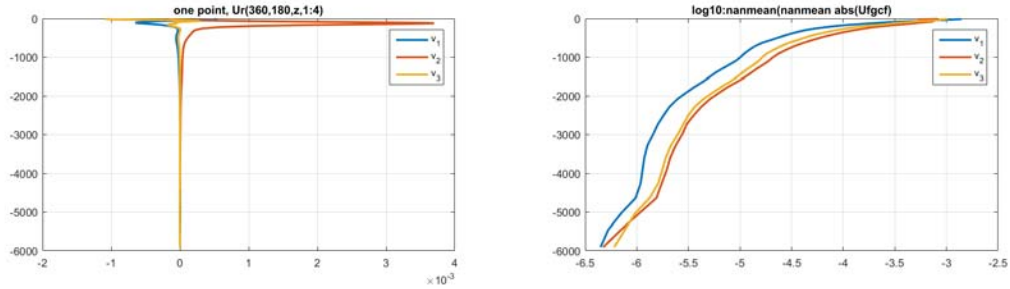


Figure 30: (Left panel) The first three singular vectors of the annual cycle in temperature as a function of depth at one point on the Atlantic equator (0°E , 0°N). (Right panel). Logarithm of the areal mean as a function of depth of the 3 singular vectors of temperature. The annual cycle in temperature is effectively confined to the top 100m of the ocean.

{temp_svd_viw}

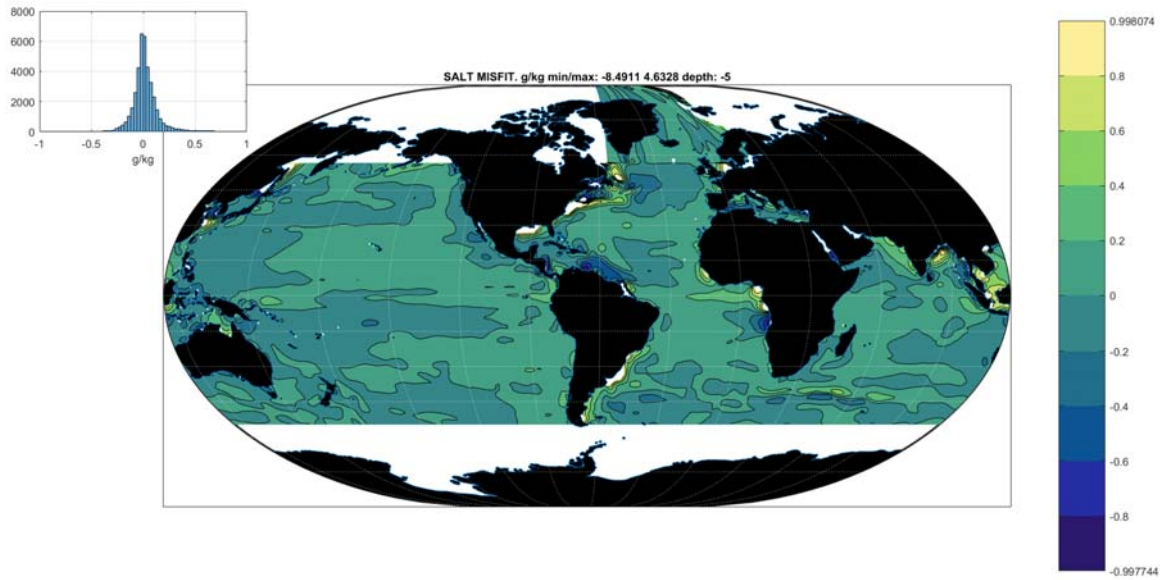


Figure 31: Misfit of the state estimate to the salinity data averaged over 20 years at 5m—effectively the surface. (g/kg).

{misfit_salt_5}

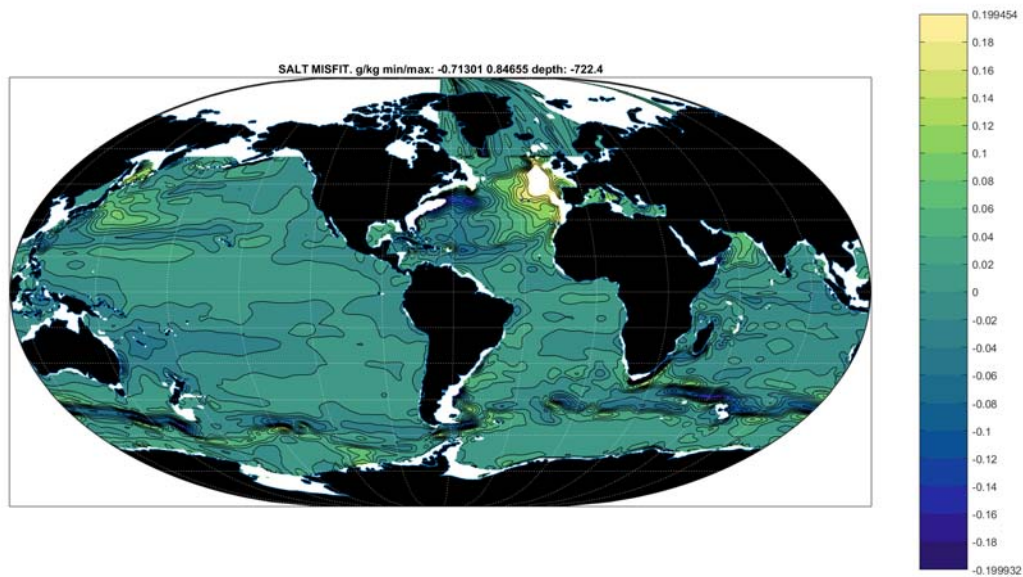


Figure 32: Same as Fig. 31 except at 722m.

{misfit_salt_7

300 *Salinity Charts*

301 A number of representative maps and sections are shown in Figs. 33-39. These are again
 302 broadly consistent with historically available estimates.

303 The global mean salinity (volume weighted) is 34.72, fortuitously identical to Worthington's
 304 (1981) estimate from a very sparse data set. Apparent changes in upper ocean salinity over 50
 305 years have been discussed e.g., by Durack et al. (2012) and Vinogradova and Ponte, (2016).
 306 The histogram of the distribution of salinity is in Fig. 40, showing the comparatively narrow
 307 range existing over the oceanic bulk.

308 **3.1 Regional Examples**

309 As an example of what can be done regionally with salinity, Fig. 41 displays the twenty-year
 310 seasonal average anomalies at 5m depth of salinity in the Bay of Bengal (see e.g., the special
 311 issue *Oceanography*, 29(2), 201) for a comparison).

312 Among other regional applications is that of Pillar et al. (2016) in the North Atlantic, and
 313 which includes a sensitivity analysis using the dual solution (see also, Part 3 of this series),
 314 Wunsch (2010) for the Indonesian Throughflow, Buckley et al. (2014, 2015) and Evans et al.
 315 (2017) for North Atlantic changes.

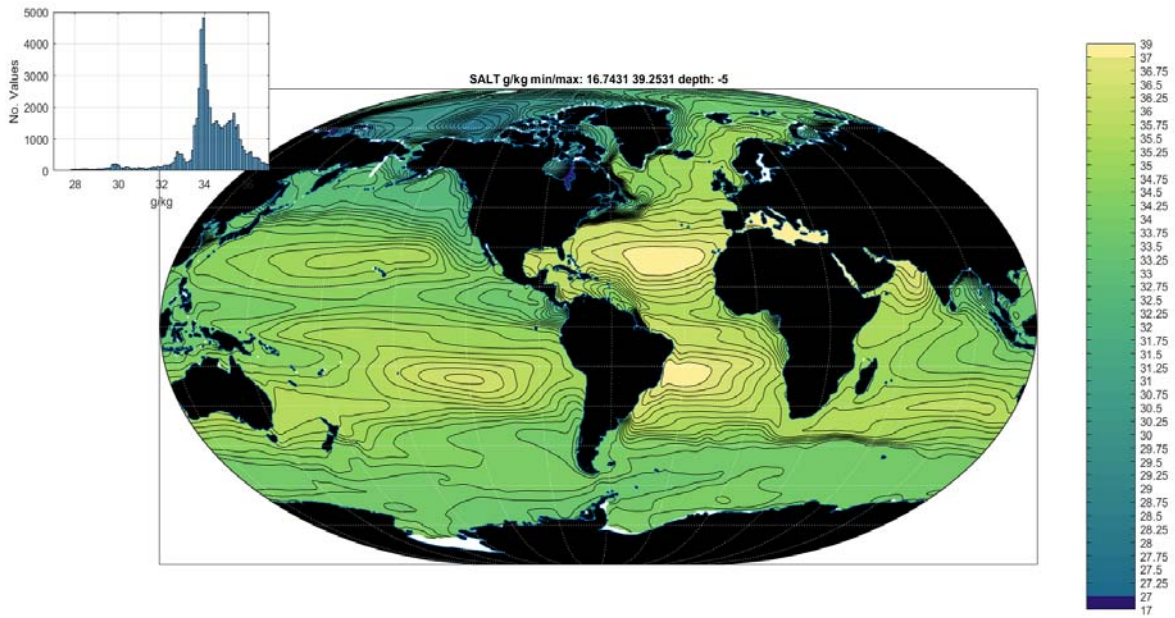


Figure 33: 20-year average salinity, g/kg, at 5m depth.

{salt_20yrmean

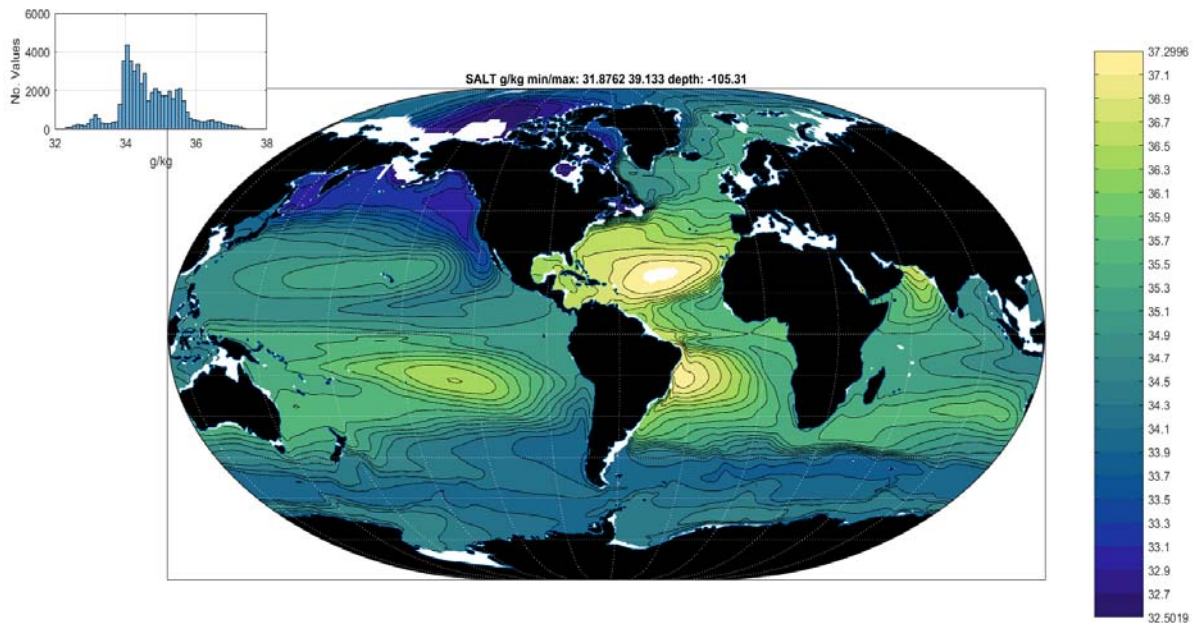


Figure 34: Twenty-year mean salinity (g/kg) at 105m depth. A marked difference with the near surface (5m) values is apparent.

{salt_20yrmean

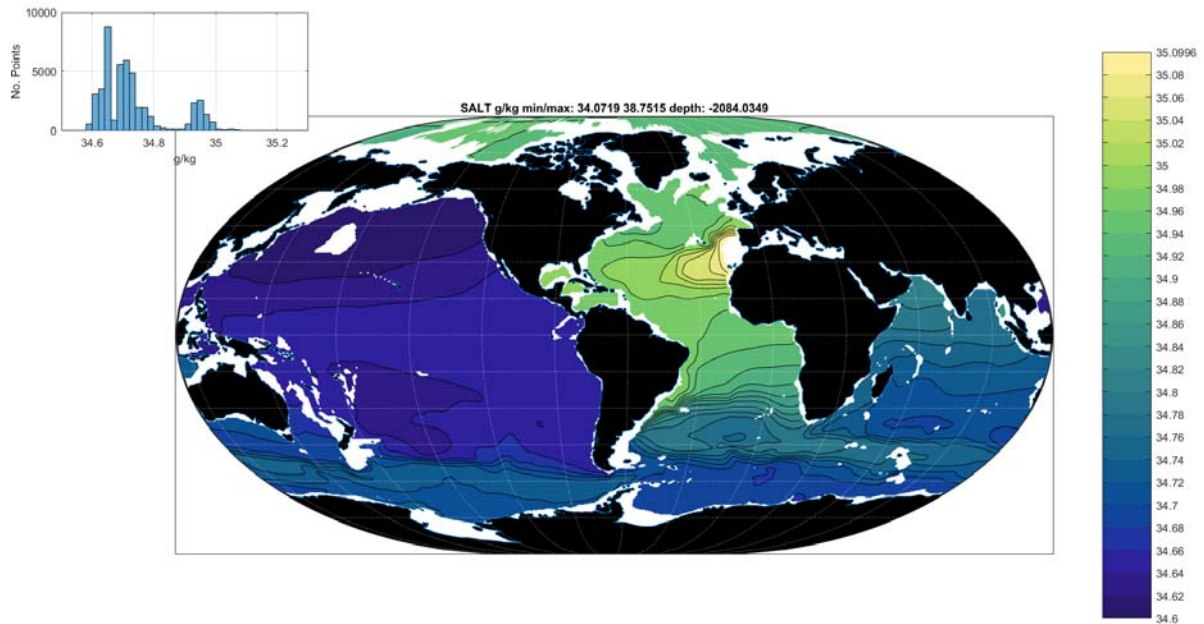


Figure 35: Twenty-year average salinity at 2100m. Excess values in the North Atlantic and the extreme of the Mediterranean Sea (values truncated here) are visible. The relatively saline Atlantic and fresh Pacific Oceans are apparent.

{salt_20yrmean}

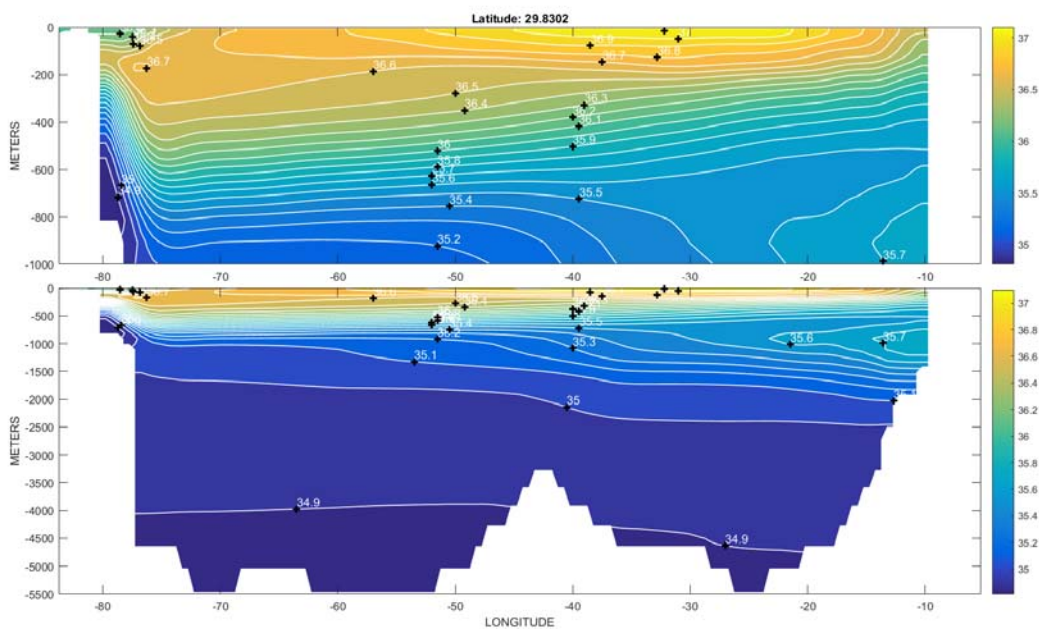


Figure 36: Twenty-year average salinity (g/kg) along a section at 30°N in the North Atlantic Ocean.

{salt_zonalsec}

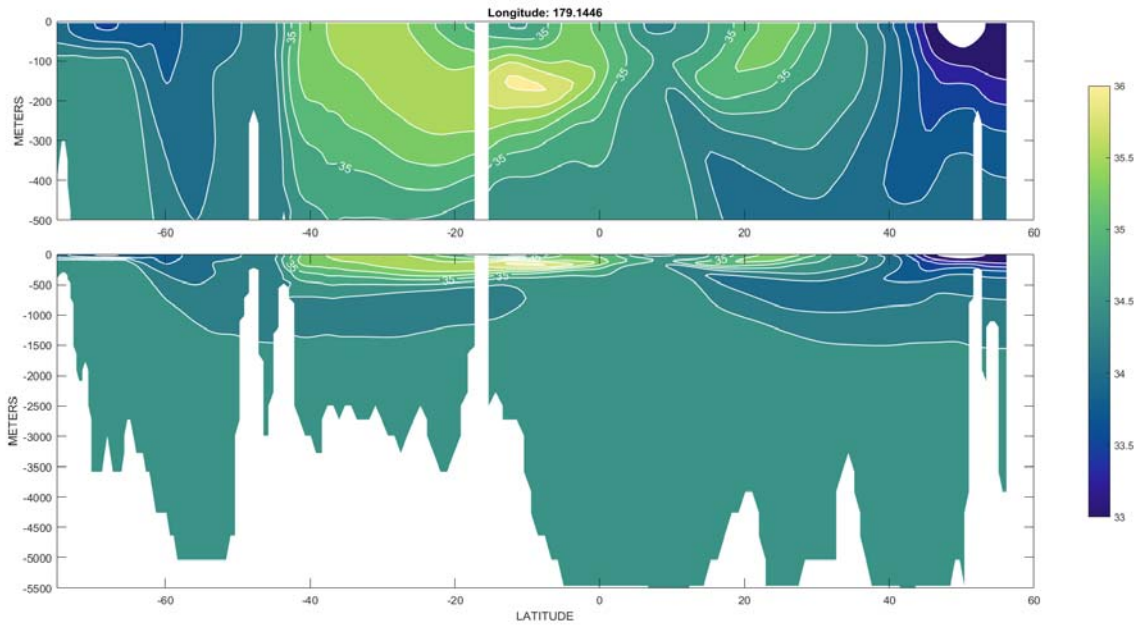


Figure 37: Meridional section of 20-year average salinity(g/kg) along 180°W in the Pacific Ocean. Note the presence of ice at the surface at the northern latitudinal extreme.

{salt_20yrmean}

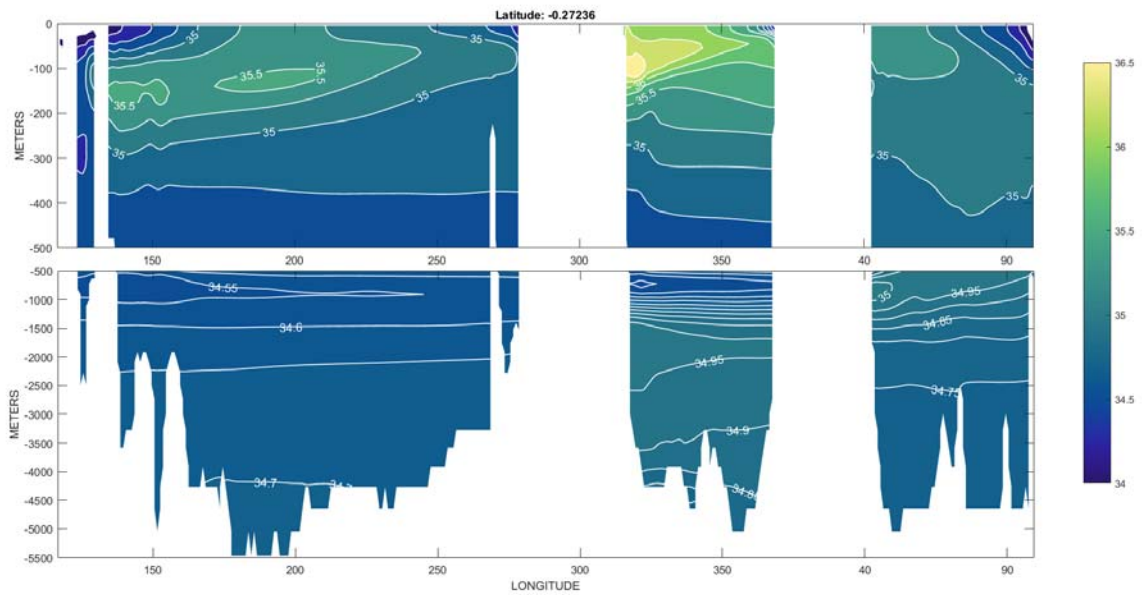


Figure 38: Twenty-year average salinity, g/kg, in a zonal section along the equator in all oceans. Note extra contours below 500m.

{salt_20yrmean}

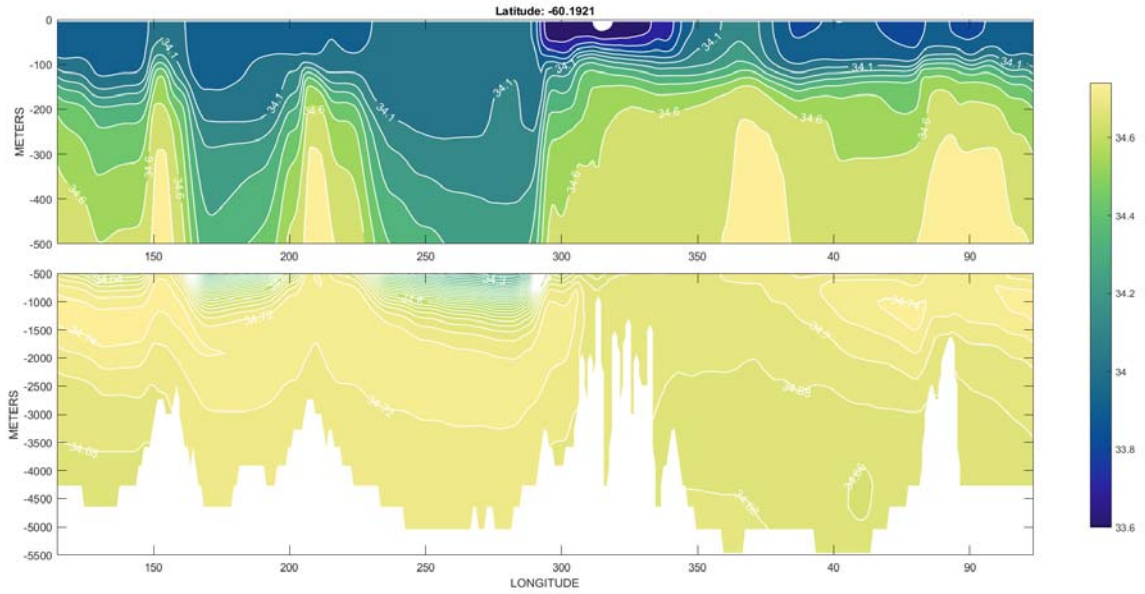


Figure 39: Twenty-year mean salinity in a zonal section through the Drake Passage with a complex zonal structure as seen also in temperature (Fig. 10) and producing a similarly complex zonally varying $T - S$ relationship in the Southern Ocean.

{salt_20yrmean}

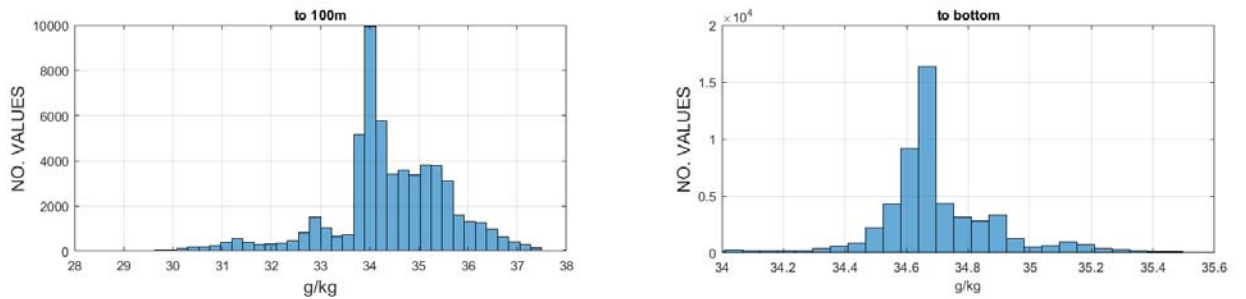


Figure 40: Histogram of salinity values averaged over the top 100m (left panel) and to the bottom (right panel). The latter is truncated so that some very small numbers of outliers are not shown.

{histo_salt_20}

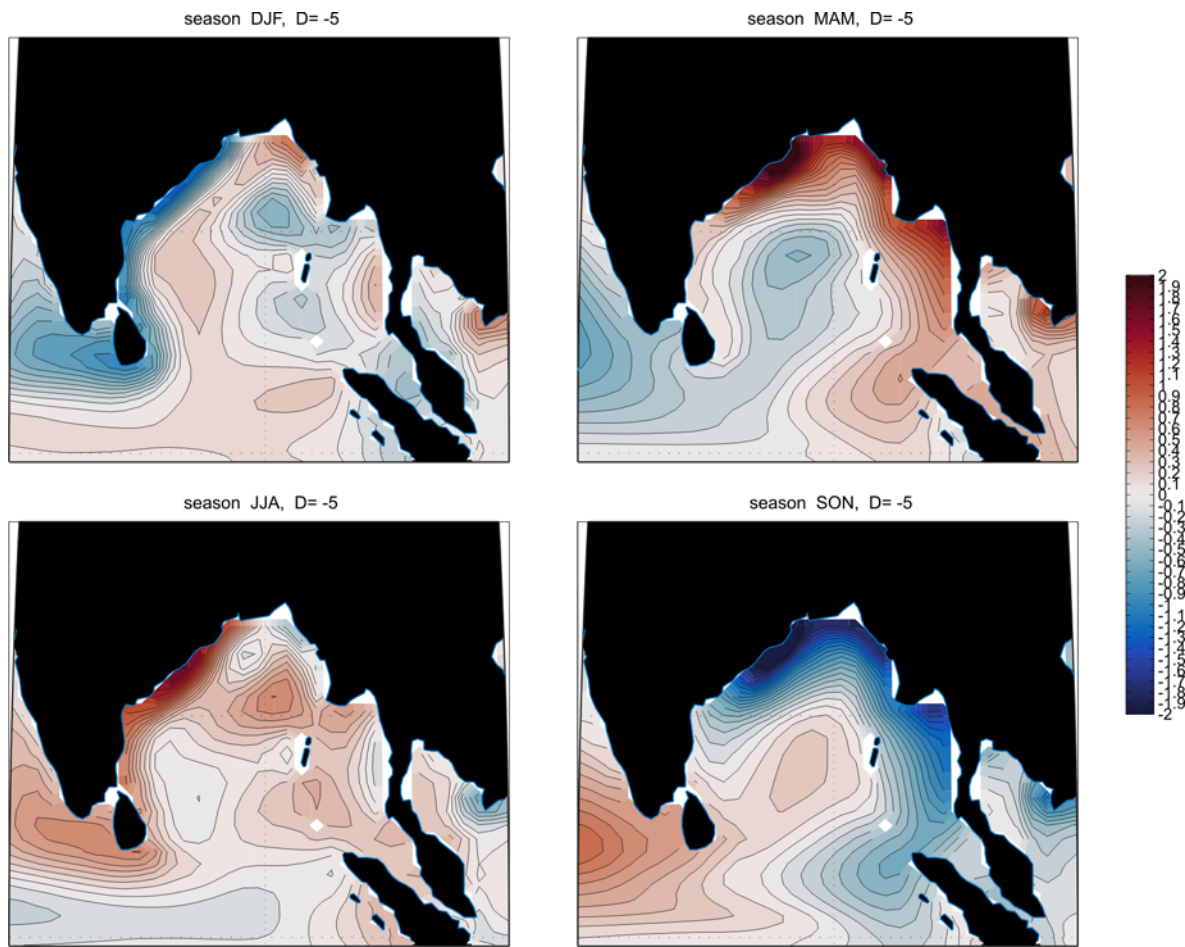


Figure 41: Twenty-year seasonal averages of salinity anomalies at 5m in the Bay of Bengal. September-November.

{bayofbengal_s

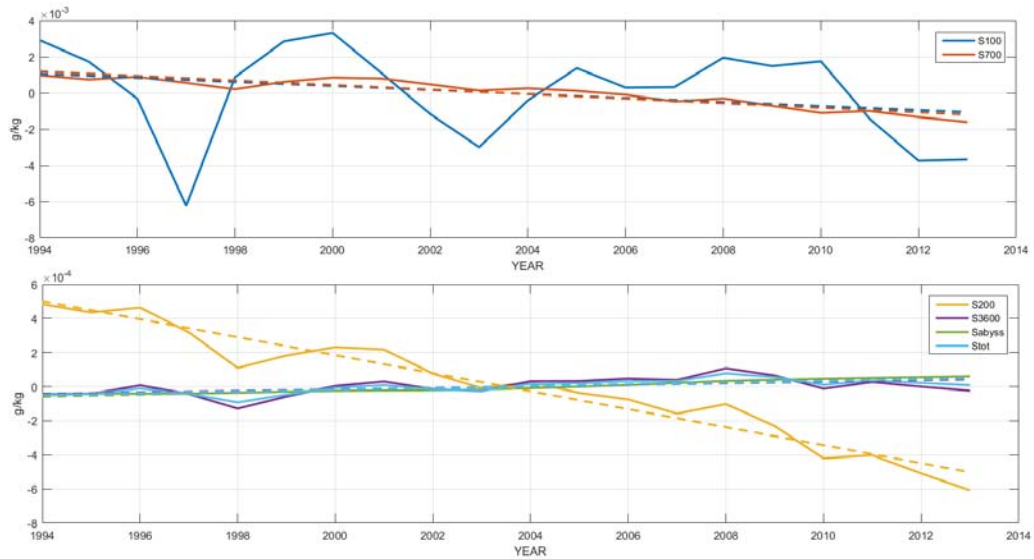


Figure 42: Salinity anomaly by year and depth interval. The upper ocean becomes fresher with a small salinity increase below 3600m corresponding to the slight net warming there and again most likely owing to the adjustment to initial conditions.

{salt_anom_byy

316 3.2 Fresh Water uptake

317 Fig. 42 shows the small changes through time occur in the salinity fields, including a weak
 318 freshening below 100m but above the abyss. The equivalent freshwater injections are shown in
 319 Table 4 as meters of water each year. The net change over 20 years to 2000m corresponds to
 320 about 3 mm/y freshwater addition or about 0.04 Sv. (For comparison, net annual precipitation
 321 over the ocean is about 12 Sv.) Spatial variations in $\partial\rho/\partial S$ were not included. If justified, more
 322 accurate calculations are obviously possible.

323 3.3 Surface Salinity Change

324 The difference between the annual mean near-surface (5 M) salinity anomalies in 2013 minus
 325 those in 1994 is shown in Fig. 43 and can be compared with the 20-year near-surface mean
 326 surface salinity in Fig. 33. Durack et al. (2012) have suggested that the surface salinity
 327 patterns over 50 years have become more intense in the last decades. In contrast with their
 328 result, the pattern correlation between the time average salinity and the 20-year difference is
 329 0.26. Even if statistically significant (not clear) the mean salinity pattern accounts for less than
 330 10% of of the spatial variation in the change; cf. Vinogradova and Ponte (2016).

Depth Range m	20 y mean Sal g/kg	Salinity Change 20 y 10^{-3} g/kg	Freshwater Input mm/y
0-100	34.74 (7.2)	-6.6	1.2
0-700	34.74 (17.2)	-2.6	3.2
0-2000	34.70 (17.1)	-1.1	3.8
0-3600	34.72 (17.0)	0	-0.1
0-bottom	34.72 (16.7)	0	-0.4
Abyss (3600m-bottom)	34.73 (11.2)	+0.1	-0.1

Table 4: Time-mean salinity in the ocean by depth range, the calculated change over 20 years, and approximate conversion to equivalent freshwater input or extraction.

{meansalt}

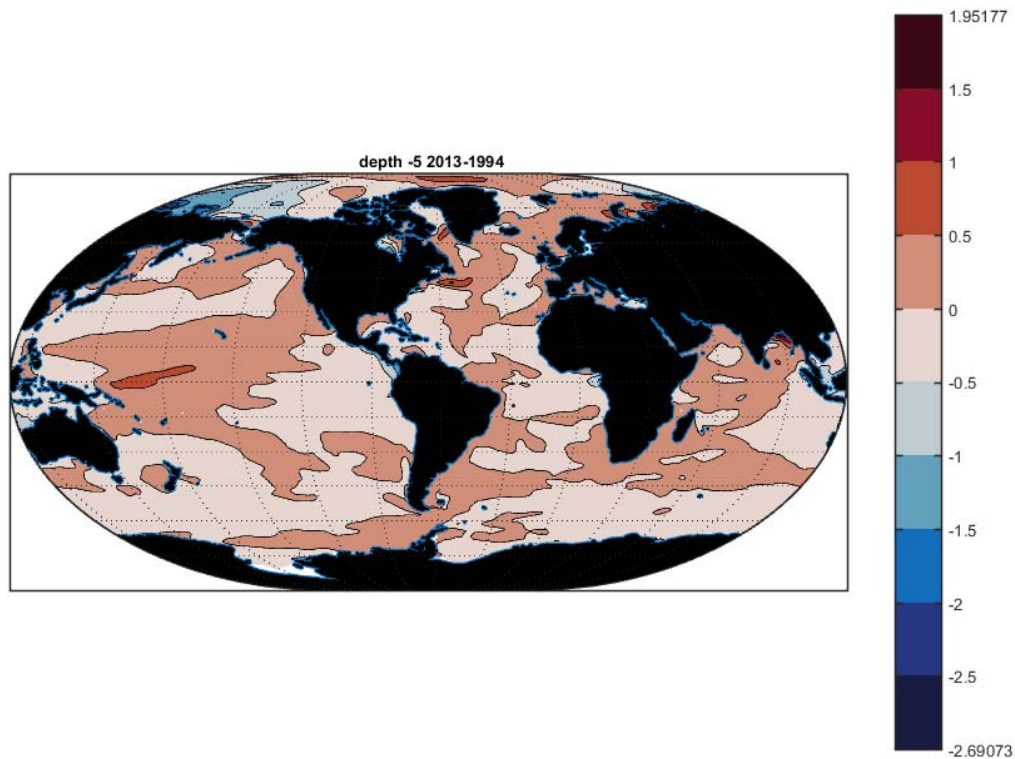


Figure 43: Change in 5m salinity between 1993 and 2014.

{salt_5m_2013_}

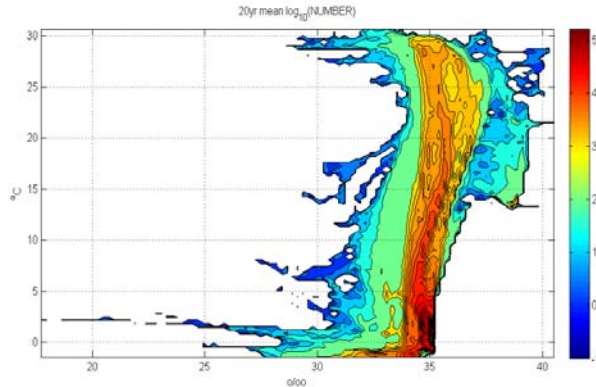


Figure 44: T-S histogram of the raw (not volume weighted) temperatures and salinities in the 20-year mean. The logarithm of the relative volume is plotted. (Cf., Fig. 3 of Wunsch and Heimbach, 2014).

{rawts_20yearm

3.4 TS-Distribution

In the 20-year average, the largest volume of water in T-S space (Fig. 44) has a temperature of 0.5°C and a salinity of 34.70 g/kg . Worthington (1981) had estimated the most abundant water in the ocean was in the intervals $1.1\text{-}1.2^{\circ}\text{C}$, $34.68\text{-}34.69\text{ g/kg}$. Separate histograms for volume weighted temperature and salinity have already been shown above.

4 Surface Elevation and Bottom Pressure

Misfits

Surface elevation, $\eta(\theta, \lambda, t)$ relative to an estimated geoid is largely, but not completely, determined by the altimetric data: the state estimate is simultaneously being fit to meteorological forcing, the thermal, salinity and ice fields, and any other data (e.g., gravity and altimeter height changes) that are present. A full determination of cause would depend upon the adjoint sensitivity of η to each of these data sets. The adjoint solution is discussed in Part 3. But because the altimetric records are the only ones nearly uniform and global over the entire 20 years, the 20-year average misfit to the time-varying altimetric measurement of η is shown in Fig. 45. Apart from some isolated outliers that have been suppressed, the misfits are generally within 10cms overall, highest at high latitudes, and showing some residual structures in the tropics. Misfits associated with the moving Kuroshio also appear.

Dynamic Topography

The 20-year mean surface elevation relative to the EGM2008 geoid (the dynamic topography; see Pavlis et al., 2012) is shown in Fig. 46. Quantitative differences exist between this estimate

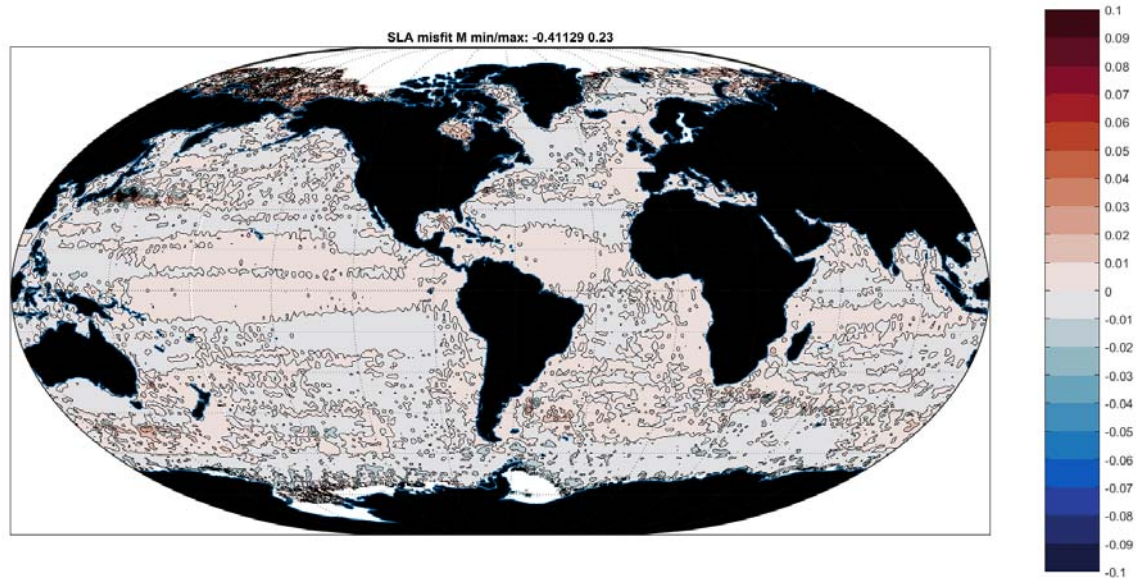


Figure 45: Average misfit (m) over 20 years of the state estimated values of η and that measured by the suite of altimeters. Based upon the average of the monthly misfits.

{slamisfit_20y

351 and the initial estimate from Rio and Hernandez (2004). Maximenko et al. (2009) published
 352 similar but different estimates based on various data sets, including surface drifter data corrected
 353 for ageostrophic effects; these latter data are not included in ECCO v4 because of concerns over
 354 the appropriate error estimates (e.g., Elipot et al., 2016).

355 Seasonal mean anomalies of η are in Fig. 47-50 and have the expected dominant hemispheric
 356 shifts. Some of the large-scale gyres, and particularly the western boundary current regions,
 357 as well as the ice-covered regions near Antarctica, show considerable seasonality. Ice-covered
 358 regions are difficult to measure whether in situ or by satellite, and high-latitude seasonal biases
 359 probably exist in all data sets. The present estimate does include some 200,000 elephant seal
 360 profiles (Roquet et al., 2013), many from under the floating ice regions.

361 The seasonal cycle in η is depicted in Figs. 47-50. Interhemispheric interchange is the major
 362 expected feature, but complex structures in the tropics remain even with 20 years of averaging.

363 Anomalies of η relative to the 20-year average in 1994 and 20 years later are shown in Figs.
 364 51, 52. One can infer a general rise in value over the 20-years, but it is highly structured.
 365 Using only tide gauges to determine the global average of figures such as Fig. 51—to a useful
 366 accuracy—is an exercise in finding a small residual in the presence of much larger spatial and
 367 temporal fluctuations.

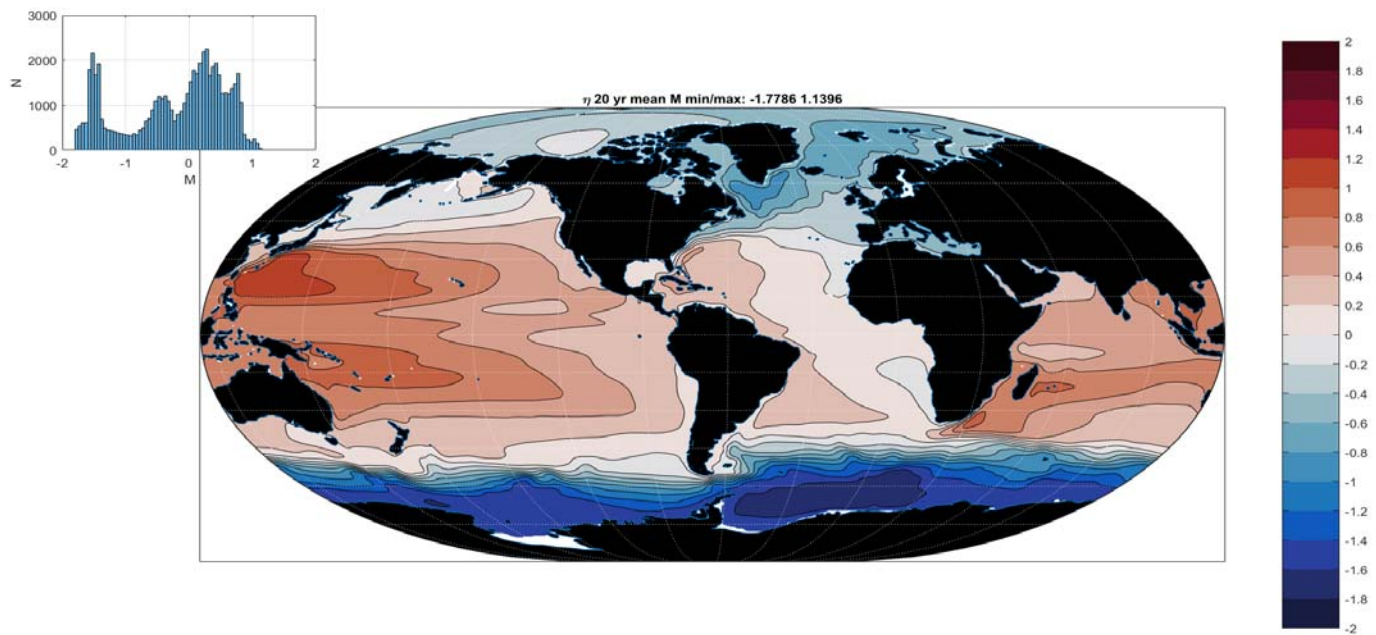


Figure 46: Twenty-year mean dynamic topography . Very low values in the ice-covered areas account separately for the ice thickness. Off-setting the entire surface by a constant would have no observable dynamical consequences. Compare to Maximenko et al. (2009), Knudsen et al. (2011). Inset shows the histogram of values about the mean.

{eta_20yearmea

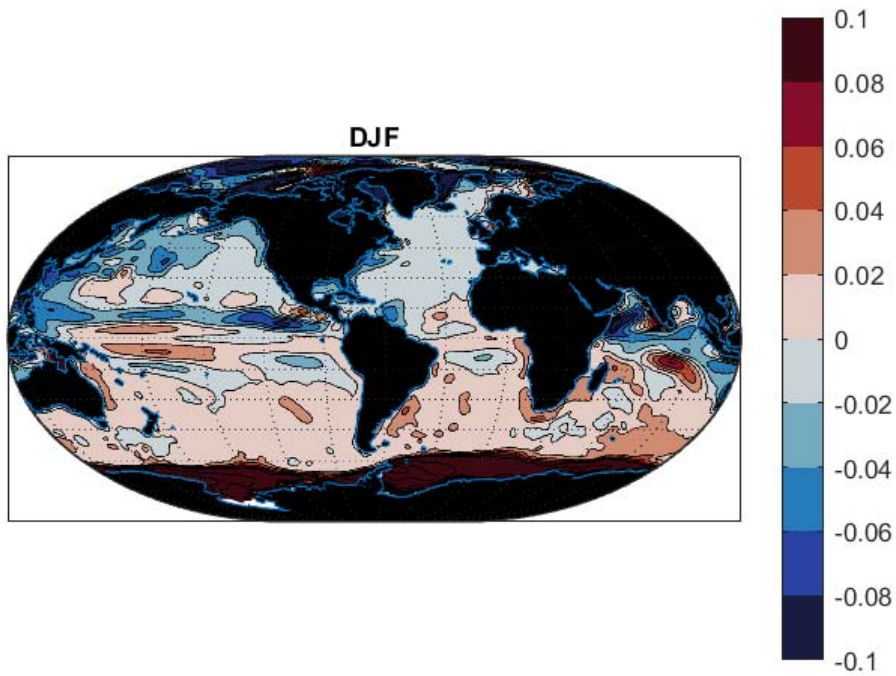


Figure 47: Twenty-year average elevation anomaly in December, January, February.

{eta_djf.tif}

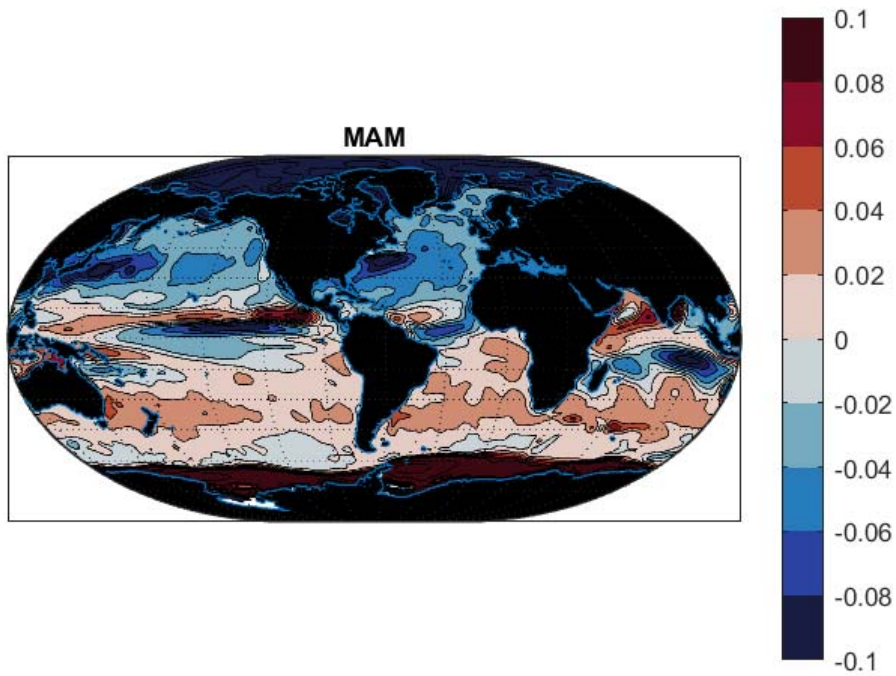


Figure 48: Same as 47 except March, April, May.

{eta_mam.tif}

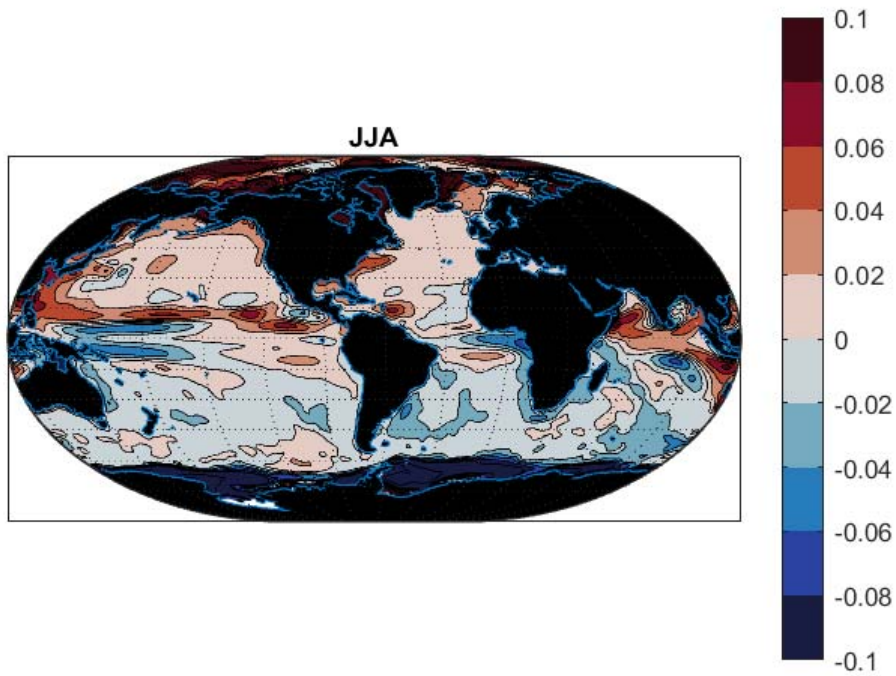


Figure 49: η anomaly, JJA.

{eta_jja.tif}

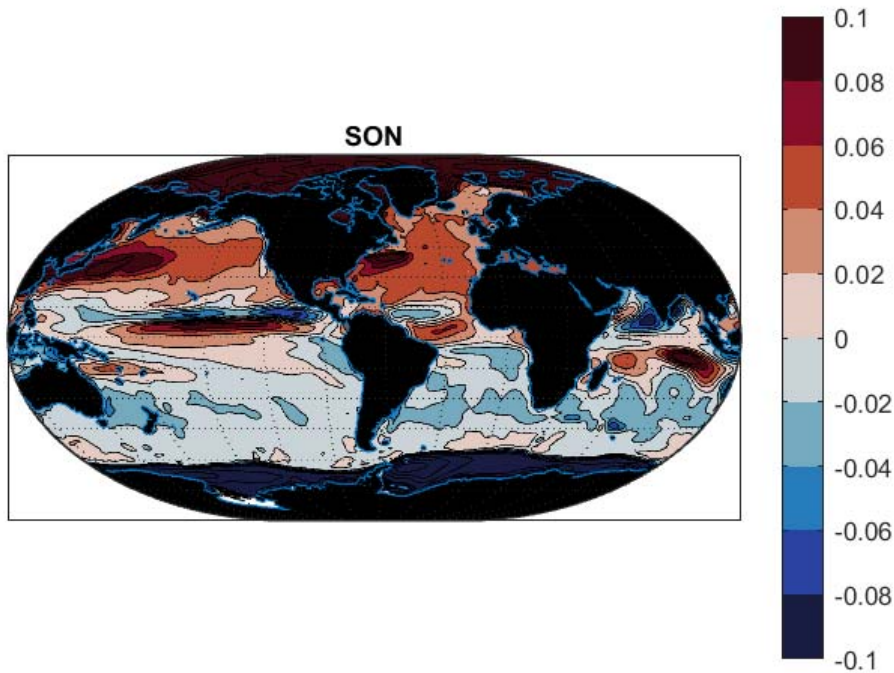


Figure 50: η anomaly September, October, November.

{eta_son.tif}

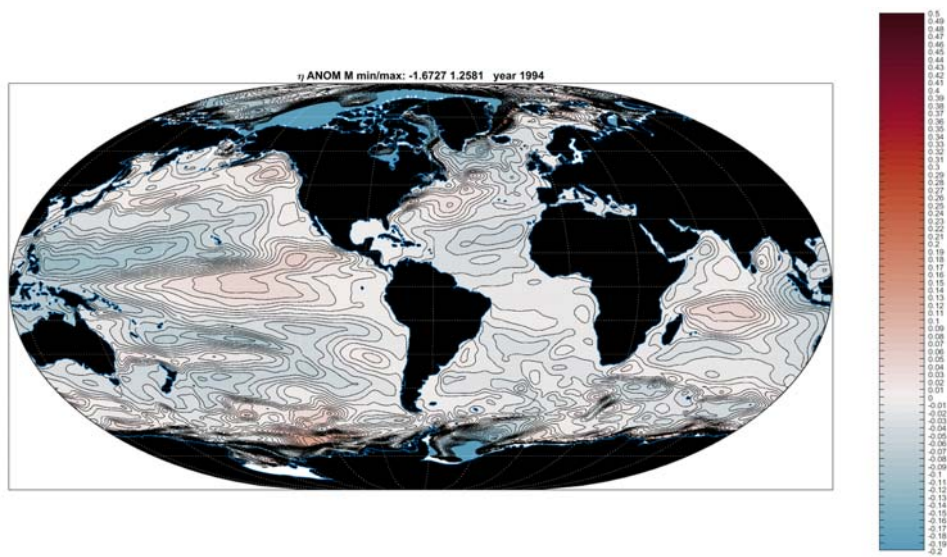


Figure 51: Anomaly (meters) of sea surface elevation η in 1994. Anomalies are relative to the mean in Fig. 46

{eta_anom_1994}

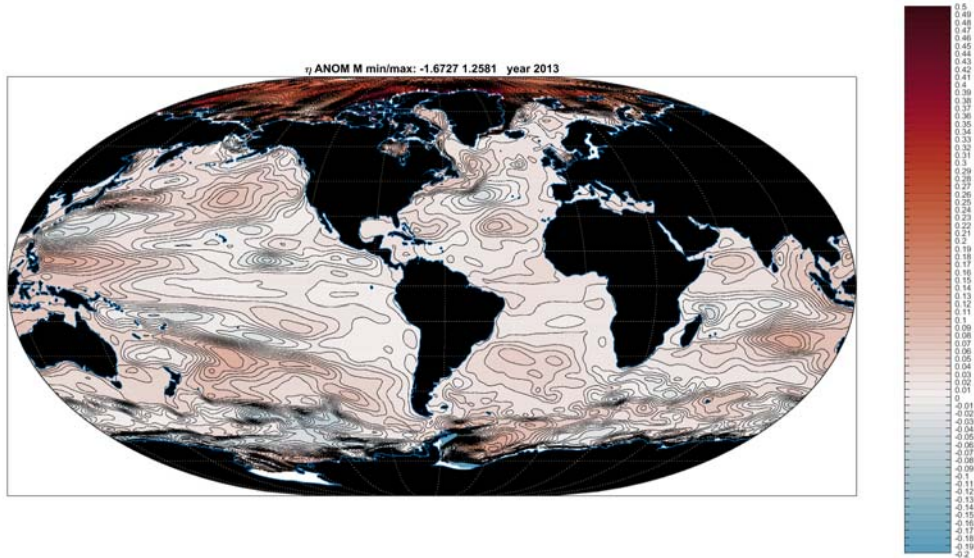


Figure 52: Anomaly of η in 2013. Compare to Fig. 51.

{eta_anom_2013}

368 *Bottom Pressure*

369 Oceanic bottom pressure, p_b , is of intense interest in the analysis of the GRACE satellite
 370 data, in studies of the rotation of the Earth, as well as in the diagnoses of sea level change (see
 371 Ponte et al., 2007; Piecuch et al., 2015). Fig. 53 displays the mean seasonal cycle, while Fig. 54
 372 indicates the change from 1994-2013 and can be compared to the estimated linear trend in Fig.
 373 55. The bottom pressure variance represents the residual about the linear trend of the yearly
 374 fluctuations. In all cases a spatial mean was removed before plotting, so that total mass change
 375 is not reflected in these plots.

376 **5 ENSO and Equatorial Structures**

377 The El Niño-Southern Oscillation (ENSO) component is, apart from the annual cycle, by far
 378 the strongest of all short-term (sub-decadal) climatic changes. Entire books have been devoted
 379 to its physics (e.g., Philander, 1990 ; Sarachik and Cane, 2010). As examples of its character,
 380 Figs. 57- 59 display the elevation and thermal anomaly at 95m and 2000m respectively during
 381 1997-2000.

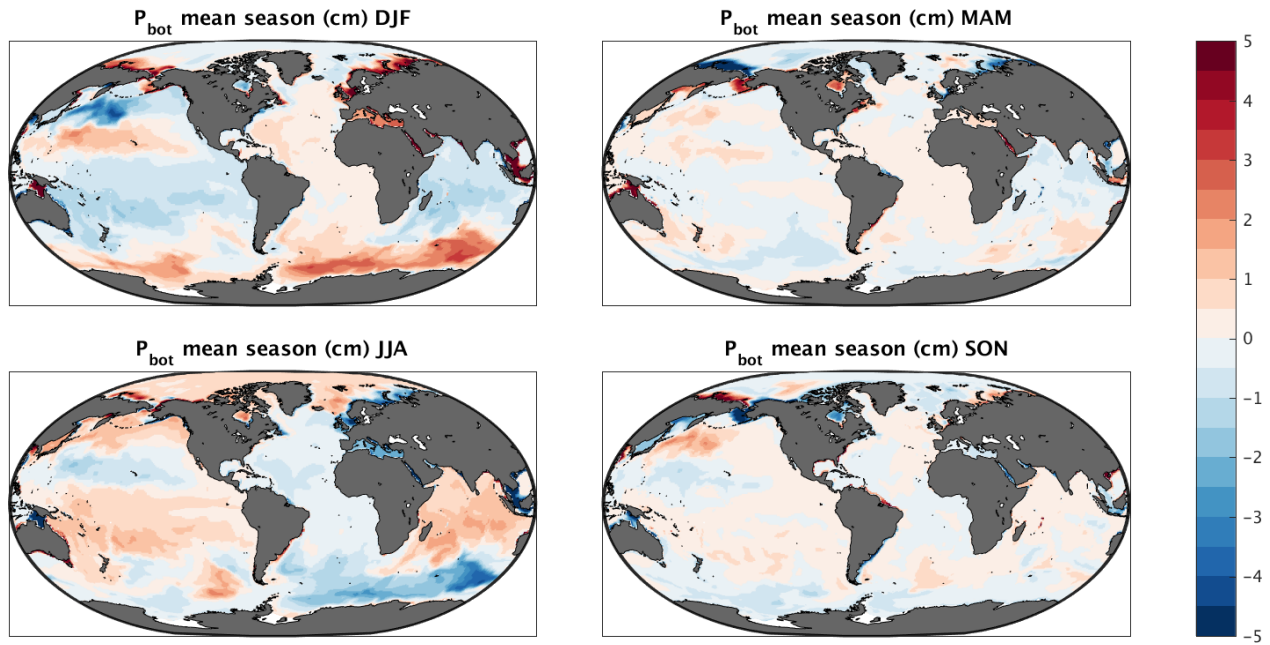


Figure 53: Twenty-year mean seasonal oscillation of bottom pressure anomaly, p_b .

{pbot_quinn_cl

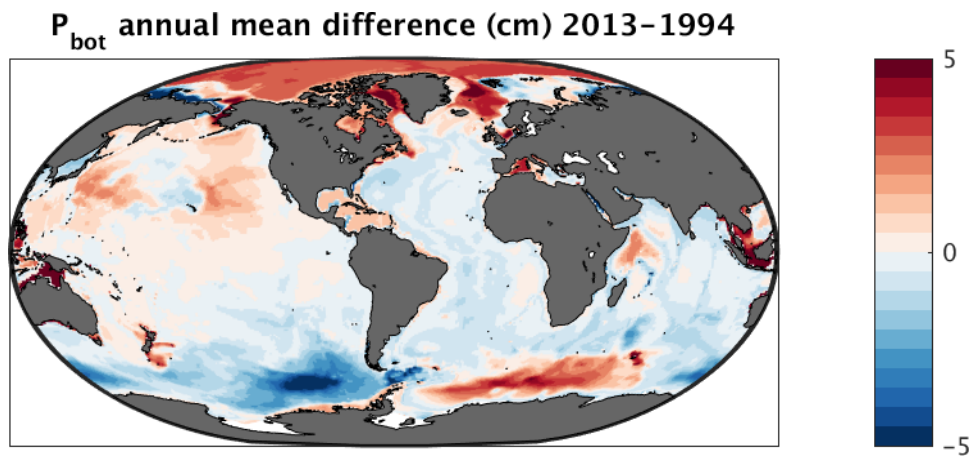


Figure 54: Bottom pressure anomaly in 2013 minus that in 1994. Spatial means removed.

{pbot_quinn_cl

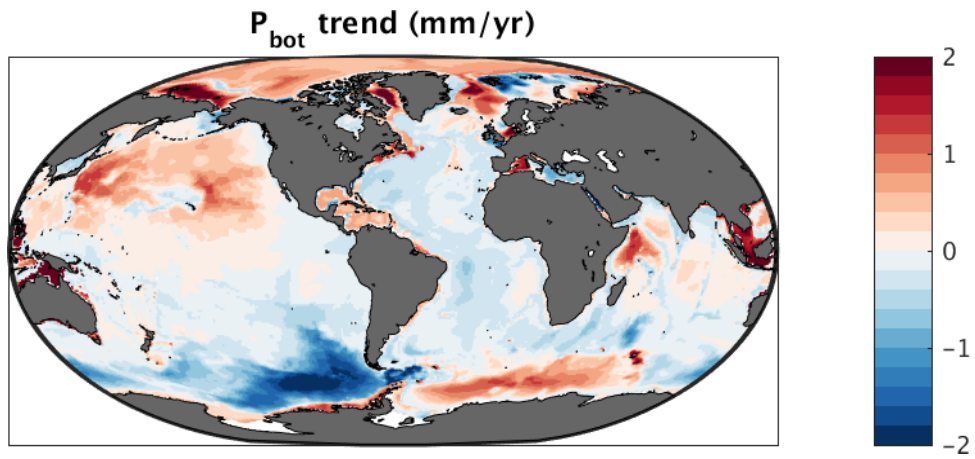


Figure 55: Linear trend (mm/y) in the bottom pressure anomaly. Compare to Fig. 54.

{pbot_quinn_cl

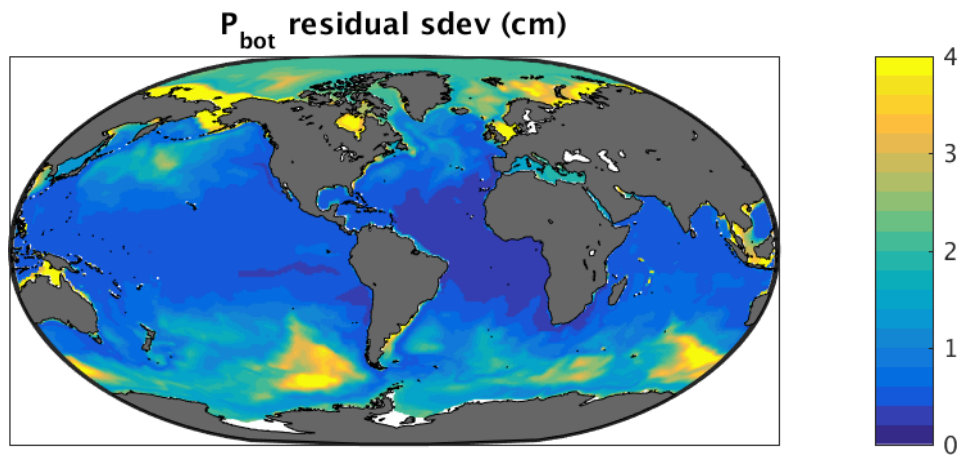


Figure 56: Standard deviation (cm) over 20 years (from annual values) of the residual bottom pressure anomaly (a linear trend estimate was removed).

{pbot_quinn_cl

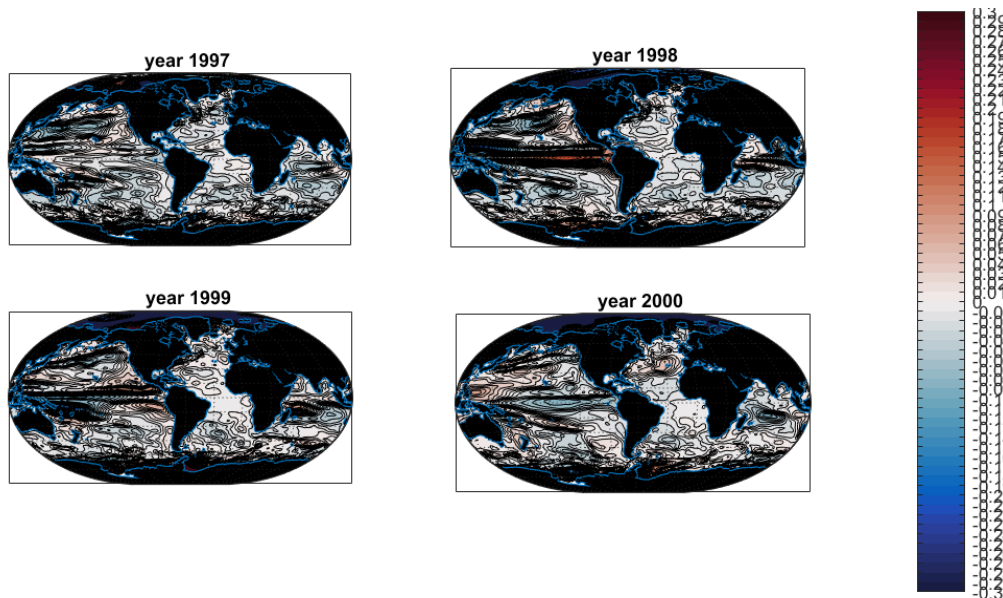


Figure 57: Annual average η (meters) for the years surrounding the 1997-1998 El Niño event. Note the Indian Ocean structure in 1998.

{eta_enso_4yea

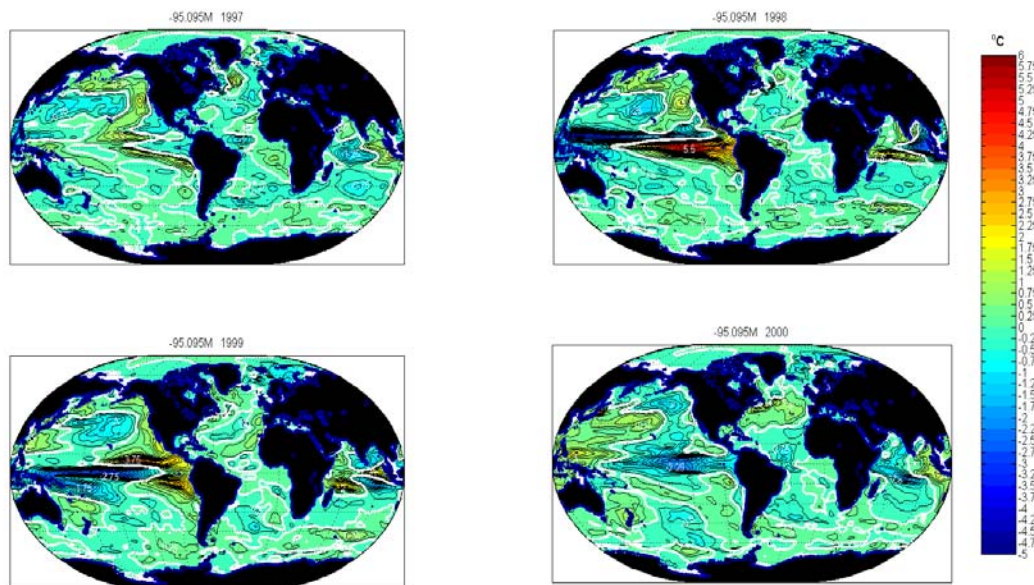


Figure 58: Annual averages at 95m of temperature in the years surrounding the 1997-1998 El Niño event.

{theta_ensoyea

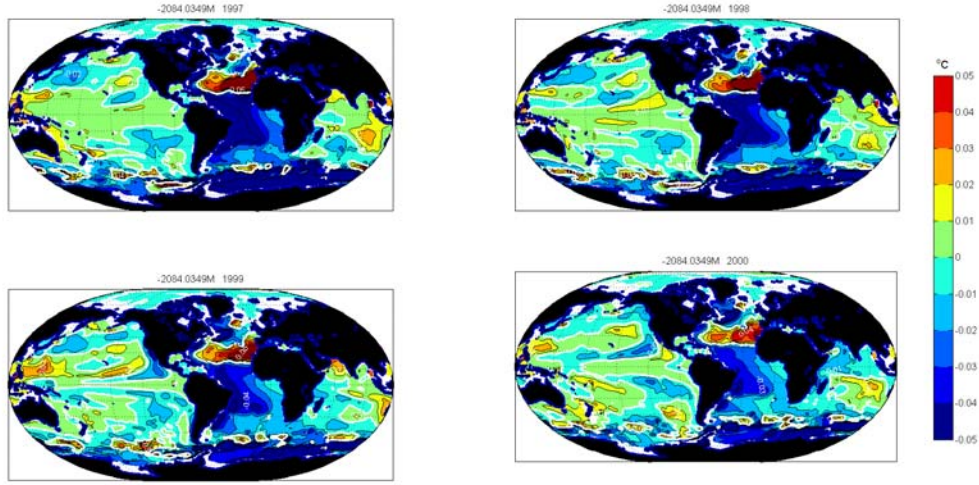


Figure 59: Same as Fig. 58 except at 2000m.

{theta_ensoyea

382 6 Mixed-Layer Depth

383 The mixed-layer depth Fig. 60 is based upon the density algorithm of Kara et al. (2003) to
 384 which comparison may be made. Fig. 61 shows the strong average seasonal response in that
 385 depth. Fig. 62 shows the 20-year mean difference in temperature between 5m and 15m and is
 386 an indication of the time-average mixed layer vertical gradient.

387 7 Buoyancy Frequency, Rossby Radii, and Equivalent Depths

388 An important dynamical consequence of a climatology is encompassed in the buoyancy frequency,
 389 $N(\phi, \lambda, z, t)$, the derived baroclinic Rossby radii of deformation R_{Di} , and the related equivalent
 390 depths, h'_j , $j = 1, 2, \dots$, where,

$$R_{Di} = \frac{\sqrt{gh'_i}}{f}. \quad (1) \quad \text{{deformationra}}$$

391 Display of N at 722m can be seen in Fig. 63 and in Wunsch (2013). Here $R_{D1,2}$ are
 392 computed from eigenvalues, γ_i , of the Sturm-Liouville problem for the flat-bottom ocean of
 393 locally constant physical depth $h(\phi, \lambda)$,

$$\frac{d^2 G_i(z)}{dz^2} + \gamma_i^2 N^2(\phi, \lambda, z) G_i(z) = 0 \quad (2)$$

394 with $w(-h) = w(0) = 0$, implying $G_i(-h) = G_i(0) = 0$. (In the interests of efficiency, the full
 395 free surface boundary condition was replaced by a rigid lid; see Wunsch, 2013 for full discussion.)

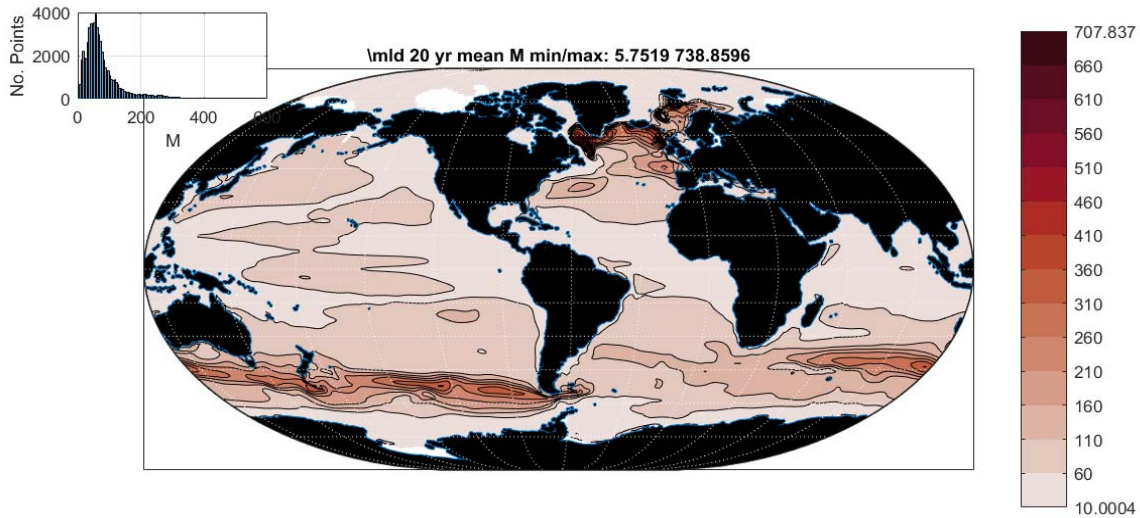


Figure 60: Twenty-year average mixed-layer depth as defined by Kara et al. (2003). Most of the ocean has values near 100m, with extreme values above 700m in the high latitude North Atlantic Ocean.

{mixed_layer_2

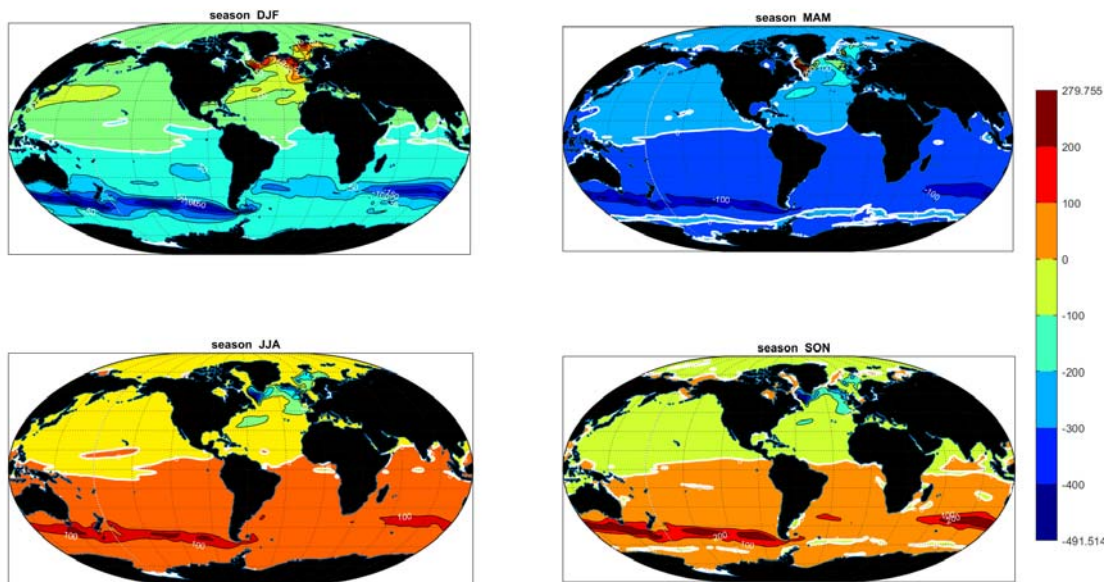


Figure 61: Anomaly of mixed-layer depth as a 20-year seasonal average. Negative values denote a shoaling relative to the mean in Fig. 60.

{mixed_layerde

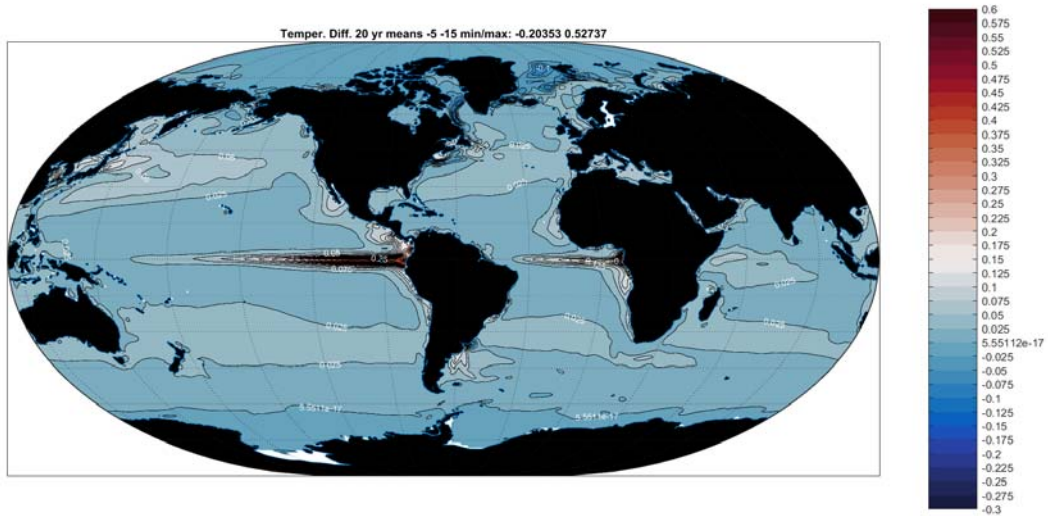


Figure 62: Difference in the temperatures at 5m and 15m as a 20 year mean. The figure is an indication of the near-surface mixed layer thermal gradient (compare Figs. 5, 6).

{temp_20yearmean}

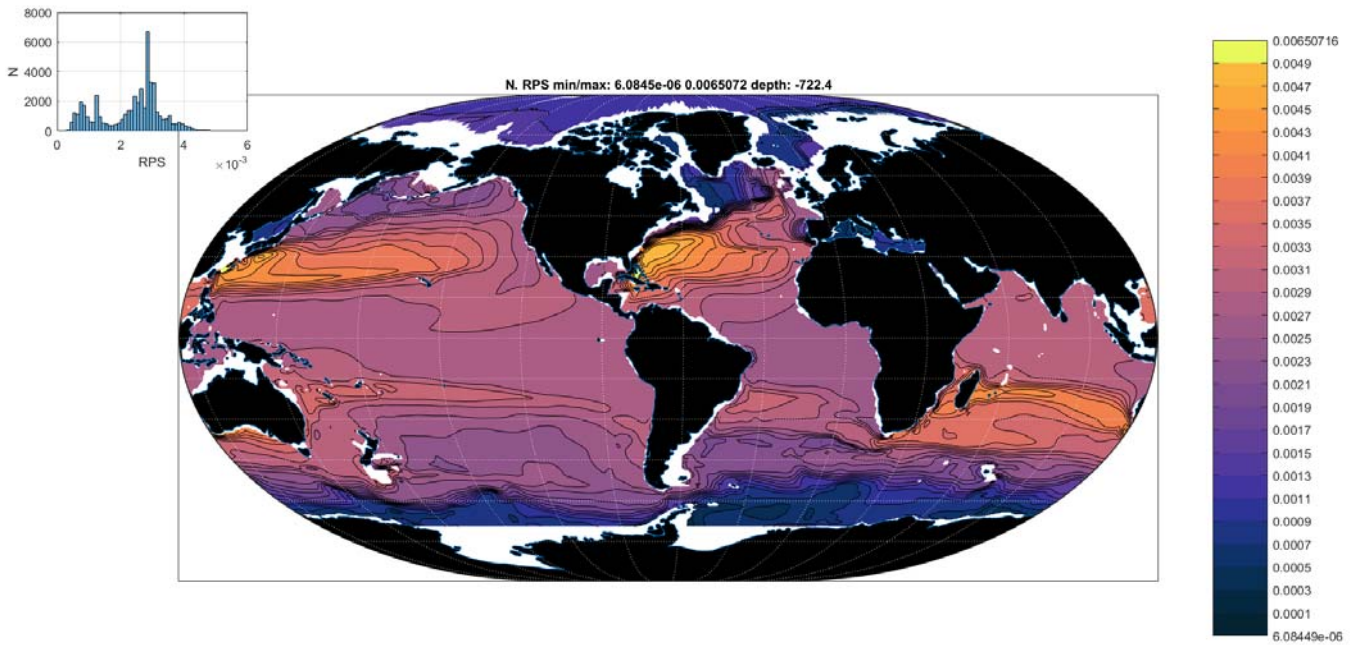


Figure 63: Estimated buoyancy frequency (N) in radians/sec at 722m as computed from the TEOS simplified formula for density and their algorithm. Estimates at other depths can be seen in Wunsch (2013).

{n_20yearavera}

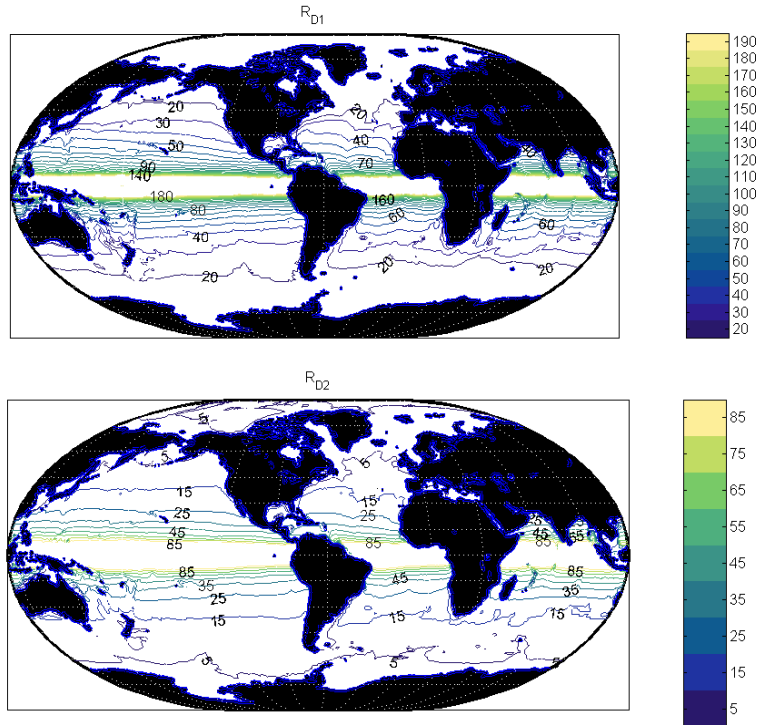


Figure 64: First and second Rossby radii, $R_{D1,2}$ computed from the solution of the rigid lid Sturm-Liouville problem. Contouring near the equatorial singularity is incomplete.

{rd1_rd2.tif}

396 Visually the chart is very similar to the earlier one of Chelton et al. (1998), but with detailed
 397 differences presumed to arise from their use of a very different climatology. Values of $G_i(0)$ are
 398 important in the interpretation of altimetric data as representing isopycnal disturbances, but
 399 the free surface boundary condition is required (which leads to a vertical velocity reversal near
 400 to the free surface). The ratio R_{D2}/R_{D1} varies between about 0.31 and 0.79 (not shown) with
 401 the smallest values at high latitudes and near the equator. A second mode weights the upper
 402 ocean differently than does the first mode and this sensitivity accounts for much of the spatial
 403 variation in the ratio. For numerical models trying to obtain realism for second and higher mode
 404 vertical structures (three or more levels or layers), resolving this second and higher deformation
 405 radius can be a serious problem.

406 The equivalent depth, h'_1 is shown in Fig. 65 and differs in detailed structure from the phase
 407 speed values $\sqrt{gh'_1}$ of Chelton et al. (1998) or Rainville and Pinkel (2006).

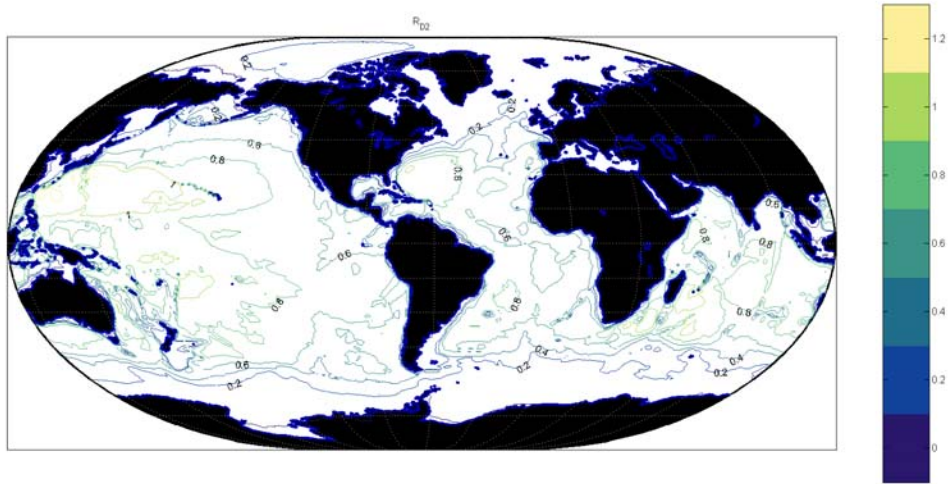


Figure 65: First equivalent depth, h'_1 , in meters. The high frequency internal wave gravity phase speed, plotted by other authors (e.g., Chelton et al, 1998; Rainville and Pinkel, 2006) from a different climatology is $\sqrt{gh'_1}$. No equatorial singularity occurs.

{h1.tif}

408 8 Comments

409 An important qualitative result of the state estimate is the spatial complexity of most variables
 410 even after 20 years of averaging (see for example, Figs. 7, 10, 39, 41). The central message must
 411 be that global space-time sampling of almost any quantity must be nearly complete—should any
 412 accurate average be required. In many variables, such as upper ocean temperature and salinity
 413 and mixed layer depth, the strong seasonal cycle must be resolved to determine the interannual
 414 changes with useful accuracies.

415 Further Parts in this series will depict the velocity field and its changes, the meteorological
 416 variables and their changes, the heat and salt transports, ice cover, a few regional comparisons,
 417 and discussion of the adjoint/dual solution and of the uncertainties.

418 *Acknowledgments*

419 Supported by NASA for the ECCO Consortium at MIT, AER, JPL. We thank all of the
 420 people, scientists, engineers, ships' crews, program managers, who finally made possible the
 421 gathering of global ocean data, as well as all those who have worked on the ECCO system and
 422 models.

References

- 424 Abraham JP, Baringer M, Bindoff NL, Boyer T, Cheng LJ, et al. 2013. A review of global
425 ocean temperature observations" implications for ocean heat content estimates and climate
426 change. *Rev. Geophys.* 51: 450-83
- 427 AchutaRao KM, Ishii M, Santer BD, Gleckler PJ, Taylor KE, et al. 2007. Simulated and ob-
428 served variability in ocean temperature and heat content. *Proceedings of the National Academy*
429 *of Sciences of the United States of America* 104: 10768-73
- 430 Adcroft A, Hill C, Campin JM, Marshall J, Heimbach P. 2004. Overview of the formulation and
431 numerics of the MIT GCM
- 432 Boyer T, Domingues CM, Good SA, Johnson GC, Lyman JM, et al. 2016. Sensitivity of Global
433 Upper-Ocean Heat Content Estimates to Mapping Methods, XBT Bias Corrections, and Base-
434 line Climatologies. *Journal of Climate* 29: 4817-42
- 435 Chaudhuri AH, Ponte RM, Forget G. 2016. Impact of uncertainties in atmospheric boundary
436 conditions on ocean model solutions. *Ocean Modelling* 100: 96-108
- 437 Chaudhuri AH, Ponte RM, Forget G, Heimbach P. 2013. A Comparison of Atmospheric Re-
438 analysis Surface Products over the Ocean and Implications for Uncertainties in Air-Sea Boundary
439 Forcing. *Journal of Climate* 26: 153-70
- 440 Chelton DB, Schlax MG. 1996. Global observations of oceanic Rossby waves. *Science* 272: 234-
441 38
- 442 Colin de Verdière A, Ollitrault M. 2016. A Direct Determination of the World Ocean Barotropic
443 Circulation. *Journal of Physical Oceanography* 46: 255-73
- 444 Dee DP, Balsameda M, Balsamo G, Engelen R, Simmons AJ, Thépaut JN. 2014. Toward a
445 Consistent Reanalysis of the Climate System. *Bulletin of the American Meteorological Society*
446 95: 1235-48
- 447 Durack PJ, Wijffels SE, Matear RJ. 2012. Ocean Salinities Reveal Strong Global Water Cycle
448 Intensification During 1950 to 2000. *Science* 336: 455-58
- 449 Elipot S, Lumpkin R, Perez RC, Lilly JM, Early JJ, Sykulski AM. 2016. A global surface drifter
450 data set at hourly resolution. *Journal of Geophysical Research: Oceans*
- 451 Forget G. 2010. Mapping ocean observations in a dynamical framework: A 2004-06 ocean atlas.
452 *Journal of Physical Oceanography* 40: 1201-21
- 453 Forget G, Campin J-M, Heimbach P, Hill C, Ponte R, Wunsch C. 2015. ECCO version 4: an
454 integrated framework for non-linear inverse modeling and global ocean state estimation. *Geosci.*
455 *Model Dev.* 8: 3071-104
- 456 Forget G, Ponte RM. 2015. The partition of regional sea level variability. *Progress in Oceanog-*

457 raphy 137: 173-95

458 Fu LL, Haines BJ. 2013. The challenges in long-term altimetry calibration for addressing the
459 problem of global sea level change. *Adv. Space Res.* 51: 1284-300

460 Fuglister FC. 1960. Atlantic Ocean Atlas of Temperature and Salinity Profiles and Data from
461 the International Geophysical Year of 1957-1958. 209 pp pp.

462 Gill AE, Niiler PP. 1973. The theory of the seasonal variability in the ocean. *Deep-Sea Res.* 20:
463 141-77

464 Gouretski VV, Koltermann, K. P. 2004. WOCE Global Hydrographic Climatology.

465 Häkkinen S, Rhines PB, Worthen DL. 2013. Northern North Atlantic sea surface height and
466 ocean heat content variability. *Journal of Geophysical Research: Oceans* 118: 3670-78

467 Kara AB, Rochford PA, Hurlburt HE. 2003. Mixed layer depth variability over the global ocean.
468 *J. Geophys. Res.* 108: 3079

469 Knudsen P, Bingham R, Andersen, O., Rio, M. H. 2011. A global mean dynamic topography
470 and ocean circulation estimation using a preliminary GOCE gravity model. *Journal of Geodesy*
471 85: 861-79

472 Koltermann KP, Gouretski VV, Jancke K, eds. 2011. Hydrographic Atlas of the World Ocean
473 Circulation Experiment (WOCE). Volume 3: Atlantic Ocean International WOCE Project Of-
474 fice, Southampton, UK, ISBN 090417557X.

475 Levitus S. 1982. Climatological Atlas of the World Ocean. 173 pp plus microfiche pp.

476 Liang X, Piecuch CG, Ponte RM, Forget G, Wunsch C, Heimbach P. 2016. Change of the Global
477 Ocean Vertical Heat Transport over 1993-2010. Submitted for publication

478 Liang X, Wunsch C, Heimbach P, Forget G. 2016. Vertical redistribution of oceanic heat con-
479 tent. *J. Clim.* 28: 3821-33

480 Marshall J, A. Adcroft, C. Hill, L. Perelman, Heisey C. 1997. A finite-volume, incompressible
481 Navier Stokes model for studies of the ocean on parallel computers. *J. Geophys. Res.*, 102:
482 5753-66

483 Maximenko N, Niiler P, Rio MH, Melnichenko O, Centurioni L, et al. 2009. Mean Dynamic
484 Topography of the Ocean Derived from Satellite and Drifting Buoy Data Using Three Different
485 Techniques. *Journal of Atmospheric and Oceanic Technology* 26: 1910-19

486 Pavlis NK, Holmes SA, Kenyon SC, Factor JK. 2012. The development and evaluation of the
487 Earth Gravitational Model 2008 (EGM2008). *J. Geophys. Res.-Solid Earth* 117

488 Pillar HR, Heimbach P, Johnson HL, Marshall DP. 2016. Dynamical Attribution of Recent
489 Variability in Atlantic Overturning. *Journal of Climate* 29: 3339-52

490 Ponte RM, C. Wunsch, Stammer D. 2007. Spatial mapping of time-variable errors in TOPEX/POSEIDON
491 and Jason-1 seasurface height measurements. *J. Atm. Oc. Tech.*, 24: 1078-85

492 Purkey SG, Johnson GC. 2010. Warming of Global Abyssal and Deep Southern Ocean Waters
493 between the 1990s and 2000s: Contributions to Global Heat and Sea Level Rise Budgets. *Jour-*
494 *nal of Climate* 23: 6336-51

495 Quinn KJ, Ponte RM. 2008. Estimating weights for the use of time-dependent gravity recovery
496 and climate experiment data in constraining ocean models. *Journal of Geophysical Research-*
497 *Oceans* 113

498 Rio MH, Hernandez F. 2004. A mean dynamic topography computed over the world ocean from
499 altimetry, in situ measurements, and a geoid model. *Journal of Geophysical Research-Oceans*
500 109

501 Roquet F, Wunsch C, Forget G, Heimbach P, Guinet C, et al. 2013. Estimates of the Southern
502 Ocean general circulation improved by animal-borne instruments. *Geophysical Research Letters*
503 40: 6176-80

504 Stammer D, Balmaseda M, Heimbach P, Kohl A, Weaver A. 2016. Ocean Data Assimilation in
505 Support of Climate Applications: Status and Perspectives. *Annu. Rev. Mar. Sci.* 8: 491-518

506 Stammer D, Wunsch C, Giering R, Eckert C, Heimbach P, et al. 2002. Global ocean circulation
507 during 1992-1997, estimated from ocean observations and a general circulation model. *Journal*
508 *of Geophysical Research-Oceans* 107: -

509 Stommel H, Arons AB. 1960. On the abyssal circulation of the world ocean-I. Stationary plan-
510 etary flow patterns on a sphere. *Deep-Sea Res.*, 6: 140-54

511 Talley LD, Feely RA, Sloyan BM, Wanninkhof R, Baringer MO, et al. 2016. Changes in Ocean
512 Heat, Carbon Content, and Ventilation: A Review of the First Decade of GO-SHIP Global Re-
513 peat Hydrography In *Annual Review of Marine Science*, Vol 8, ed. CA Carlson, SJ Giovannoni,
514 pp. 185-215

515 Vinogradov SV, Ponte RM, Heimbach P, Wunsch C. 2008. The mean seasonal cycle in sea level
516 estimated from a data-constrained general circulation model. *Journal of Geophysical Research-*
517 *Oceans* 113

518 Vinogradova NT, Ponte RM. 2016. In search for fingerprints of the recent intensification of the
519 ocean water cycle. *J. Clim.* (submitted)

520 Vinogradova NT, Ponte RM, Fukumori I, Wang O. 2014. Estimating satellite salinity errors for
521 assimilation of Aquarius and SMOS data into climate models. *Journal of Geophysical Research-*
522 *Oceans* 119: 4732-44

523 Wunsch C. 2016. Global Ocean Integrals and Means, with Trend Implications In *Annual Review*
524 *of Marine Science*, Vol 8, ed. CA Carlson, SJ Giovannoni, pp. 1-+

525 Wunsch C, Heimbach P. 2013. Dynamically and kinematically consistent global ocean circula-
526 tion state estimates with land and sea ice In *Ocean Circulation and Climate*, 2nd Edition, ed.

527 JC G. Siedler, W. J. Gould, S. M. Griffies, Eds., pp. 553-79: Elsevier
528 Wunsch C, Heimbach P. 2014. Bidecadal thermal changes in the abyssal ocean and the obser-
529 vational challenge. *J. Phys. Oc.* 44: 2013-30